Article

Pyrite Characteristics in Lacustrine Shale and Implications for Organic Matter Enrichment and Shale Oil: A Case Study from the Triassic Yanchang Formation in the Ordos Basin, NW China

Qianshan Zhou, Jiangyan Liu, Bo Ma, Chao Li, Yueye Xiao, Guojun Chen, and Chengfu Lyu*

Read Online

ACCESS | 📊 Metrics & More | 📰 Article Recommendations

ABSTRACT: Pyrite is widely distributed in lacustrine shales and has become a research focus in unconventional oil and gas exploration. Pyrite morphology is useful for identifying different types of organic matter and assessing shale oil enrichment in organic-rich shale. Abundant pyrite is developed in the source rocks from the Chang 7 Member of the Yanchang Formation in the Ordos Basin, NW China. However, the relationship between different pyrite types and the differential enrichment of shale oil still needs to be clarified. The organic geochemistry, petrology, and isotopic composition of the Chang 7 Member samples were analyzed. The significance of pyrite types and sulfur isotopic compositions as indicators of depositional environments and shale oil enrichment was emphasized. The Chang 7 shales contain three pyrite morphologies, framboidal pyrite (type A), spherulitic pyrite (type B), and euhedral and anhedral pyrite (type C),

Pyrite types — Effects on organic types — Effects on shale oil enrichment

and their aggregates. The sulfur isotopic compositions of pyrite ($\delta^{34}S_{py}$) in Chang 7 shales with different pyrite types exhibited regular patterns. The $\delta^{34}S$ values of types A, B, and C pyrites were sequentially positive overall (average values are −2.739, 2.201, and 7.487‰ in sequence), indicating that type A pyrite was formed during the syn-sedimentary to early diagenetic stage and types B and C pyrites were formed during the early to middle diagenetic stage. Types A, B, and C pyrites showed sequentially increasing kerogen type index values and kerogen carbon isotope values (mean values of −31.59, −28.70, and −26.45‰, successively), indicating that the horizons where types A, B, and C pyrites developed correspond to types I, II, and III organic matter, respectively. Strong correlations between the pyrite content and oil components reveal that pyrite indicates shale oil enrichment. Moreover, variations in pyrite type significantly influenced the enrichment behavior of shale oil. Types A and B pyrites contributing to reservoir space showed shale oil enrichment. They promoted saturated hydrocarbon enrichment at >15% pyrite content, whereas type C pyrite did not indicate shale oil enrichment. These findings provide new insights into the differential enrichment of organic matter and shale oil and valuable guidance for the large-scale exploration and development of shale oil resources.
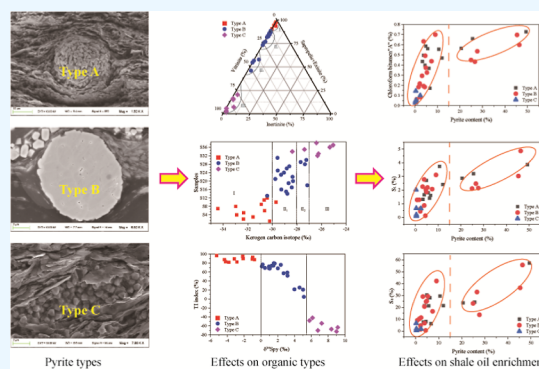
1. INTRODUCTION

The continuous advancement of theories and technologies in oil and gas exploration and development, the growing global demand for oil and gas, and shale oil have drawn attention worldwide.[1−8] The abundance, type, maturity, and preservation conditions of organic matter influence the hydrocarbon generation potential of the source rocks. Shale is a common source rock, primarily composed of quartz and clay minerals with additional feldspar, calcite, and pyrite. Variations in the mineral composition play a crucial role in hydrocarbon generation, expulsion capacity, reservoir physical properties, shale brittleness, and shale oil and gas accumulation. Specifically, pyrite, a prevalent authigenic mineral in shale, exhibits distinct distribution patterns that indicate the enrichment and preservation of organic matter and its catalytic effect on hydrocarbon generation. Furthermore, the favorable positive correlations between framboidal pyrite content, total

organic carbon (TOC) content, and pyrolyzed free hydrocarbon (S_1) content indicate a close relationship between pyrite formation and organic matter content.[9] However, previous studies focused on framboidal pyrite. Whether other pyrite types, such as spherulitic, euhedral, and anhedral pyrite, indicate organic matter enrichment remains uncertain.
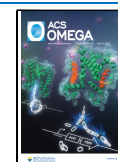
Iron ions play a vital role in organic matter deposition, with higher iron ions associated with organic matter enrichment and preservation.[10,11] Studies of the size of framboidal pyrite and TOC indicated that framboidal pyrite plays a significant role in
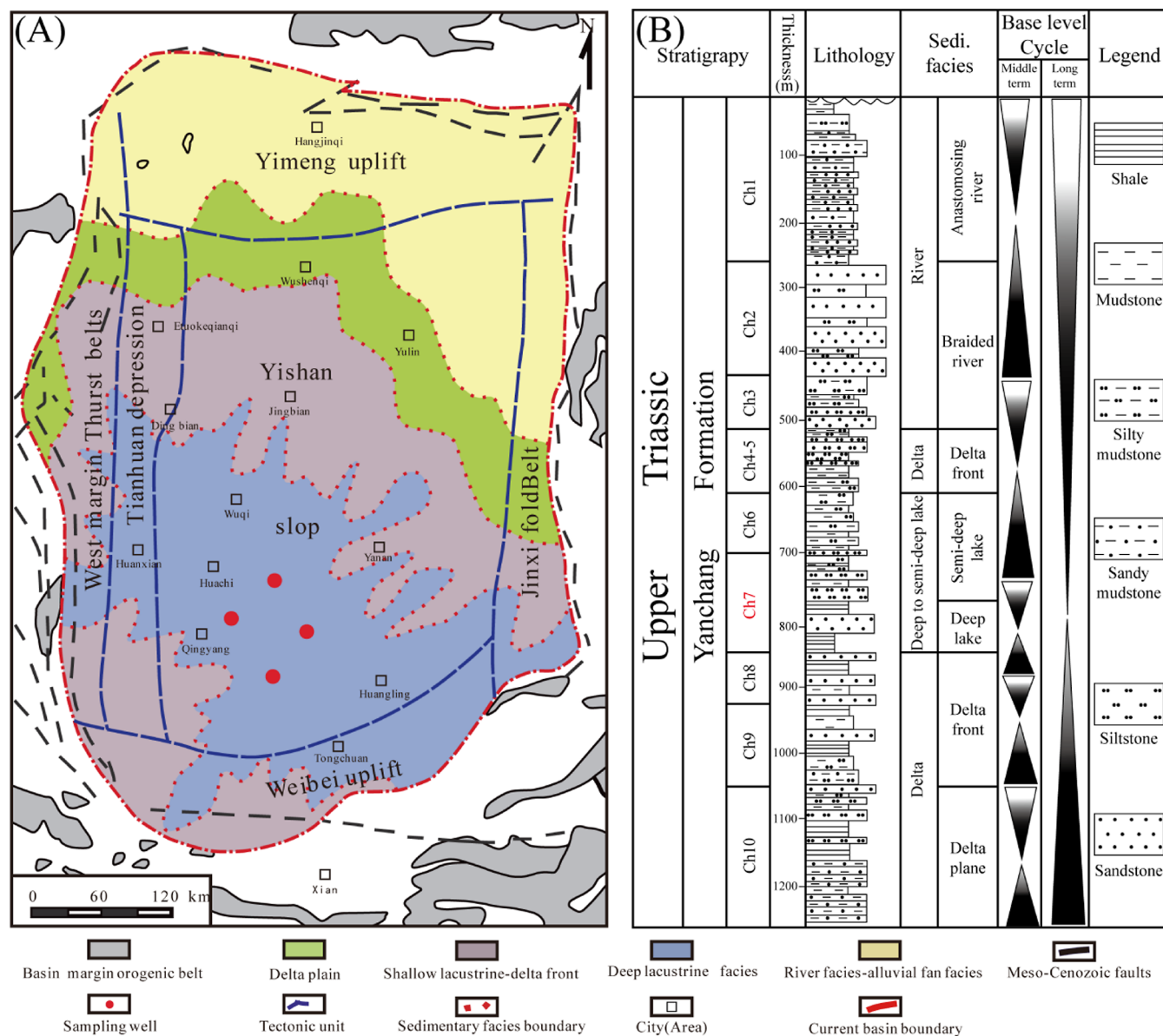
Figure 1. (A) Tectonic division of the Ordos Basin and well location [adapted with permission from ref 62 Copyright (2022) (Science China Press)]. (B) Sequence stratigraphic framework of the Upper Triassic Yanchang Formation.

promoting organic matter enrichment.[12−14] Based on the formation period and the developmental mechanism, sedimentary pyrite in shale are categorized into three types: syn-sedimentary, diagenetic, and postfilling pyrite.[15−19] Pyrite in different morphologies is found in lacustrine shales, including framboidal, spherulitic, layered, nodular, euhedral, and anhedral pyrites. Understanding the formation stages of these different pyrite forms is crucial to investigate whether they can serve as indicators of organic matter enrichment. Currently, sulfur isotope analysis of pyrite is considered the most effective method for elucidating the genetic processes of pyrites and inferring environmental changes during pyrite formation.[20−26] During the syn-depositional stage, the $\delta^{34}S$ values of pyrite show a significant loss formed due to the action of bacterial sulfate reduction. The $\delta^{34}S$ values of pyrite formed during early diagenesis are similar to those of SO_4^{2-}-reduced sulfides. Due to the Rayleigh fractionation effect, the $\delta^{34}S$ values of pyrite formed in the late diagenesis stage will gradually increase.[27−31] Therefore, the pyrite formation period was determined

according to the difference in sulfur isotopes in different pyrite forms. Framboidal pyrite is generally considered to have formed during syn-sedimentary and early diagenetic stages, with a small grain size and negative sulfur isotopes. In contrast, spherulitic, euhedral, and anhedral pyrites may have formed during diagenesis when framboidal pyrite microcrystals increase in size or directly crystallize in sulfur-bearing waters when the concentration of reactive iron is low, with a large grain size and negative sulfur isotopes.[12,32−37] In addition, Taotao et al. (2018) used scanning electron microscopy (SEM) to determine that type I and type II organic matter constituted an organic/pyrite complex with framboidal pyrite, forming a group around pyrite in the core as a whole, which was conducive to liquid hydrocarbon enrichment. In contrast, type III organic matter mostly appeared as contours and framboidal pyrite was rare.[9] Jizhen et al. (2014) found that the pyrite content in type III organic matter of Longtan Formation shale in southern Sichuan was significantly lower than that of marine type I Barnett shale and Woodford shale.[36] Lin et al.

(2017) reported that the pyrite content in sapropelic organic source rocks was very high and that the organic matter type will affect the pyrite content.[21] Bian (2024) investigated the continental shales of the Chang 7 Member and concluded that the formation and transformation of organic matter are prerequisites for the formation of pyrites.[38] Thus, a high framboidal pyrite content corresponds to a high organic matter content and sapropelic organic matter, which in turn correspond to a high hydrocarbon potential. However, this was based on the relationship between framboidal pyrite and organic matter types in marine shales, observed by using SEM. The relationship between different pyrite types and organic matter in lacustrine shales has not yet been investigated. Moreover, the role of varying pyrite types and their contents in shale oil enrichment in lacustrine shales is uncertain.

In recent years, the distribution of pyrite in marine organic-rich shale has become an indicator for shale oil and gas enrichment areas, with good results in the Barnet Shale of Fort Worth Basin, North America, and the Longmaxi Formation in the Jiaoshiba, Weiyuan, Wulong, and Pengshui areas of the Sichuan Basin, China.[12,14,18,39] Jingwei et al. (2013) observed the presence of asphaltene molecules on the surface of pyrite using atomic force microscopy. Fluorescence microscopy showed that pyrite fluoresced in the intercrystalline pores of framboidal pyrite, while pyrite did not show fluorescence after cementation.[40] Framboidal pyrite surfaces and intercrystalline pores were essential for liquid hydrocarbon accumulation.[40] Yuhong et al. (2016) also found that abundant liquid hydrocarbons existed in framboidal pyrite, and the energy-dispersive spectrometry (EDS) determined the carbon content to be 44.35%, indicating that framboidal pyrite had a high enrichment effect on liquid hydrocarbons.[41] Taotao et al. (2018) used SEM to analyze framboidal pyrite in low- to high-maturity shale and found the surface and pores of framboidal pyrite filled with liquid hydrocarbons.[9] These liquid hydrocarbons indicate that framboidal pyrite plays a positive role in promoting shale oil enrichment. The effects of pyrite on the generation of hydrocarbon from organic matter have been studied widely. Numerous catalytic hydrocarbon generation experiments of pyrite on kerogen or shale have confirmed that both the pyrite generated in shale and the pyrite added to shale can accelerate the pyrolysis reaction rate by reducing the apparent activation energy of the pyrolysis reaction or increase the pyrolysis reaction, which can promote the early decomposition of organic matter and significantly increase the generation of liquid hydrocarbons at 50 °C in advance.[42,43]

Accordingly, widespread pyrite in shales indicates the enrichment and preservation of organic matter and shale oil's formation and enrichment process. It is an ideal carrier for revealing the enrichment mechanism of organic matter and the distribution of shale oil. However, studies on the significance of different types of pyrite in lacustrine shales as indicative of organic matter abundance, type, and differential enrichment of shale oils are relatively scarce and lack systematic evidence. Therefore, to elucidate the types of pyrite in lacustrine shales, the formation environment, and the significance of varying types of pyrite on shale oil enrichment, a systematic study is required on the influence of different pyrite types on the organic matter richness, type, and shale oil enrichment for exploration and development.

This study sampled and observed the organic-rich shale section of the Chang 7 Member from the Triassic Yanchang Formation in the Ordos Basin to determine the organic geochemistry, pyrite morphology and content, and the relationship between shale oil and pyrite was analyzed using Rock-Eval pyrolysis, chloroform extract, TOC content, total sulfur (TS) content, kerogen maceral, kerogen carbon isotopes ($\delta^{13}C_{kerogen}$), X-ray diffraction (XRD), field-emission scanning electron microscopy (FE-SEM), and sulfur isotopic composition of pyrite ($\delta^{34}S_{py}$) analysis. The formation stages and characteristics of different pyrite types were clarified, and the influence of different pyrite types on organic matter enrichment was discussed. Based on this, combined with the distribution characteristics of shale oil, the relationship between different pyrite types and shale oil distribution and the influence of pyrite on shale oil enrichment are discussed.

2. GEOLOGICAL BACKGROUND

The Ordos Basin is a large superimposed basin located in central China with an area of 370,000 km^2 (Figure 1). The accumulated proven geological reserves of shale oil submitted in the basin are 11.53×10^8 t.[44] According to the structural characteristics of the basin, the basin is divided into six secondary tectonic units: Weibei uplift, Yishan slope, Tianhuan depression, Yimeng uplift, western margin thrust belt, and Jinxi fold belt. In the Paleozoic, the basin was a marine and marine-terrigenous craton basin, and it evolved into a terrestrial lake basin in the Mesozoic. The sedimentary characteristics of the Triassic Yanchang Formation record the evolution of the subsidence of the Ordos Basin. Approximately 1000−1300 m of continental clastic sediments were deposited during the Upper Triassic Yanchang Formation sedimentary period. According to the lithology and marker layer difference, the Yanchang Formation consists of 10 members (from bottom Chang 10 to top Chang 1) (Figure 1). Among them, the sedimentary period of the Chang 7 Member is the heyday of the development of the inland depression lake basin with an area of 65,000 km^2. It deposited a set of organic-rich shale and dark mudstone with thin layers of powder-fine sandstone. The shale layer system is mainly composed of organic-rich shale and dark mudstone with a thickness of nearly 110 m.[45]

The Chang 7 Member of the Triassic Yanchang Formation in the Ordos Basin is the main shale oil-producing reservoir of the Changqing oilfield. The minerals of fine-grained sedimentary rocks mainly include quartz, potassium feldspar, plagioclase, calcite, dolomite, pyrite, and clay minerals.[46,47] By comparison of the statistics of pyrite content in different strata of different basins, it is found that the pyrite content of fine-grained sedimentary rocks in the Chang 7 Member of the Triassic Yanchang Formation in the Ordos Basin is generally high.

According to the statistical results of samples from the Ordos Basin, except for the pyrite content of fine-grained sedimentary rocks in the Chang 7 Member of the northwest lake basin that is less than 5%, the pyrite content in other areas of the lake basin is more than 20%, with a high pyrite content and various types.[47] The pyrite development section is often a shale oil enrichment section, an ideal object for studying the differential enrichment of shale oil by pyrite of different origins.

3. SAMPLES AND ANALYTICAL METHODS

Due to the widespread distribution and relatively high pyrite content of the organic-rich black shales in the depositional center of the Ordos basin, a total of 38 black shale samples were collected from cores of four wells in the Chang 7 Member
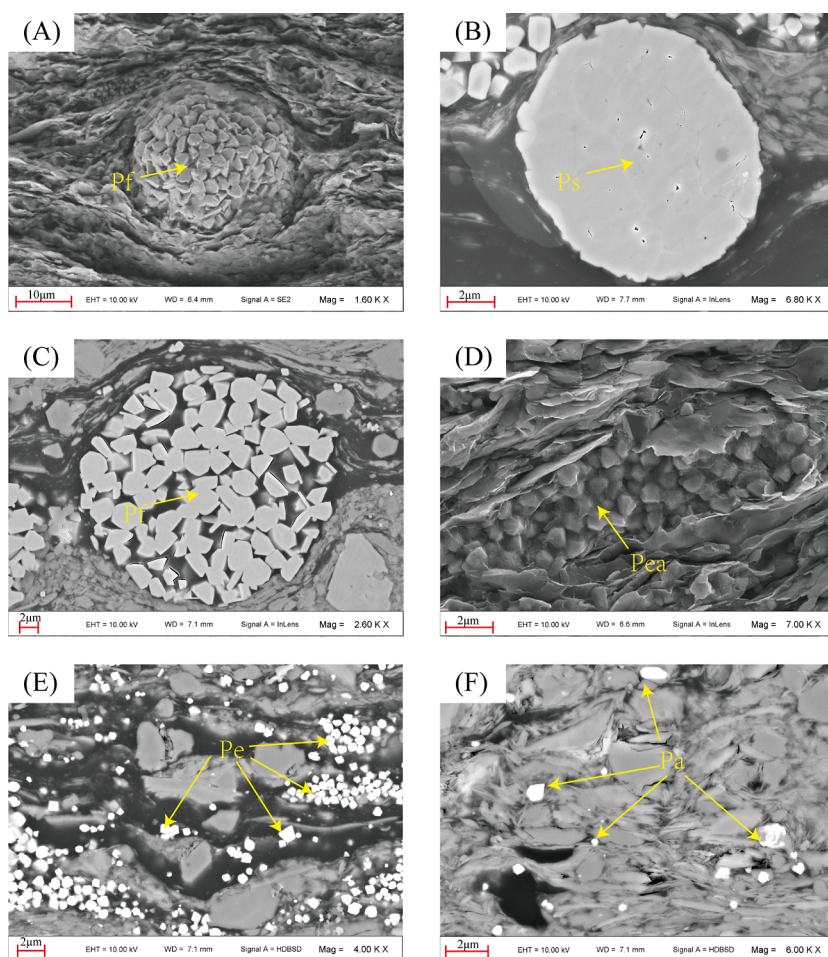
Figure 2. FE-SEM observation of pyrites in the Chang 7 Shale. (A) Framboidal pyrite, intercrystalline pores develop, Sample 6, 2060.26 m; (B) spherulitic pyrite, dissolution pores develop, Sample 22, 2067.61 m; (C) framboidal pyrite, organic matter filled in the intercrystalline pores, Sample 7, 2071.82 m; (D) euhedral pyrite aggregates, Sample 33, 1968.72 m; I euhedral pyrite, Sample 36, 1989.38 m; (F) anhedral pyrite, Sample 38, 2001.09 m. Abbreviations: Pf = framboidal pyrite; Ps = spherulitic pyrite; Pea = euhedral pyrite aggregates; Pe = euhedral pyrite; Pa = anhedral pyrite.

of the Yanchang Formation in the central Ordos Basin (Figure 1), which are the main shale oil production zones. The core samples were air-dried after removing surface stains, after which they were divided into seven separate sections for analyses of XRD, TOC, TS, FE-SEM, $\delta^{34}S_{py}$, kerogen maceral, kerogen carbon isotopes ($\delta^{13}C_{kerogen}$), Rock-Eval pyrolysis, and chloroform bitumen "A" and oil components.

Samples were ground to 200 mesh for XRD, TOC, TS, and Rock-Eval measurements. One part of powdered samples was flattened in a sample tank, after which the tank was placed in an X-ray diffractometer for mineral composition analysis. The XRD analysis was performed on a Japan Rigaku Ultima IV diffractometer with a Ni filter and Cu Kα radiation, with the X-ray tube operated at 40 kV and 50 mA. Each scan was taken from 2 to 60°, with a step interval of 0.02° at a rate of 2.0°/min. The specific experimental methods were described by Zhou et al., 2022.[48] The second part of powdered samples (10 mg) was placed in a porcelain crucible, and hydrochloric acid was added to remove carbonate, after which the crucible was heated on a hot plate at 60 °C for more than 2 h. The crucible was washed with distilled water to neutrality, cooled, and dried, and then placed in a LECO CS-344 carbon–sulfur analyzer for TOC and TS analysis. The experimental methods were described by Chen et al., 2020.[49] The third part of the

powdered samples (30−50 mg) was placed in a crucible and pyrolyzed in a Vinci Rock-Eval 6 Turbo device to obtain free hydrocarbon (S_1), pyrolyzed hydrocarbon (S_2), T_{max}, TOC, etc. Detailed description of Rock-Eval pyrolysis can be found in Behar et al., 2001.[50]

A portion of the fresh sample was cut into blocks and later polished by Ar ion milling for FE-SEM and EDS analyses. The images were obtained on a Quanta FEG-450 FE-SEM instrument equipped with an EDS microprobe (Bruker Quantax 200 X Flash 6/30 detector). Pyrite crystals were identified by their bright color in the backscattered electron mode and their EDS characteristics. The operation method and steps are described by Zhou et al., 2022.[48]

Kerogen isolation was performed using the traditional acid treatment method according to Liu et al., 2022.[51] Samples crushed to the size of a pea were first placed in a plastic beaker, and HCl was added to remove carbonates. The solution was washed to neutrality with distilled water, and then HF was added to remove silicates, after which the solution was washed to neutrality with distilled water. The acid-treated samples were sieved through a 10 μm nylon mesh to remove small debris and then transferred to test tubes for centrifugation. Finally, the obtained kerogen was prepared as a thin section to observe and count the relative content of each maceral under a

Table 1. Mineral Composition of Shale Samples from the Chang 7 Member

sample	depth/m	mineral composition (%)								
		quartz	plagioclase	potash feldspar	calcite	dolomite	ankerite	siderite	pyrite	total clay
S1	2035.42	52.29	10.16	9.36	0.91	1.08	2.46	0.1	10.6	13.04
S2	1910.23	50.06	2.90	1.58	0.64	6.25	0	0.52	6.22	31.83
S3	2044.06	35.56	18.88	4.45	0	0	1.16	0.79	4.43	34.73
S4	2048.12	36.59	10.31	2.58	0	11.15	0	1.16	6.69	31.52
S5	2058.31	31.93	16.69	4.39	0	0	1.08	1.43	25.56	18.92
S6	2060.26	42.16	13.55	3.06	0	0	0	1.05	12	28.18
S7	2071.82	14.97	9.47	3.83	0	0	1.05	1.07	49.33	20.28
S8	2079.38	25.58	18.78	2.79	0	2.08	0	0.69	20.56	29.52
S9	2080.26	25.55	25.73	17.29	8.52	1.22	0	3.07	3.32	15.3
S10	1984.13	48.80	12.70	1.54	0	0	0	0.85	3.85	32.26
S11	1967.29	43.56	15.88	7.55	19.14	0.39	0.72	0	4.83	7.93
S12	1969.52	45.45	24.32	11.19	0.68	0.35	0.78	0	5.62	11.61
S13	2005.16	26.31	13.50	3.57	0.75	0.91	1.23	0.71	26.61	26.41
S14	2006.08	50.78	8.74	2.05	0	0	0.43	0.85	24.91	12.24
S15	2007.22	70.64	8.18	6.62	0	0.63	0.81	0.25	7.35	5.52
S16	2034.48	23.17	5.69	2.05	1.84	0.87	0	1.06	46.33	18.99
S17	2041.22	32.85	3.71	3.29	0	0.56	0.51	0	27.68	31.4
S18	1986.15	50.53	7.20	1.61	0.95	1.56	0.87	0.62	3.83	32.83
S19	1972.39	47.58	3.05	1.33	8.68	4.59	1.02	0.85	5.31	27.59
S20	2507.37	50.27	2.80	1.45	7.65	6.49	0.89	0.51	0.73	29.21
S21	1965.66	38.75	6.96	1.76	0	16.14	0	2.18	4.35	29.86
S22	2067.61	16.45	12.33	6.02	0	0	0.97	0.8	45.32	18.11
S23	1977.48	47.07	2.30	2.02	0.5	0.99	0	0.79	4.56	41.77
S24	1980.96	44.99	3.11	1.54	0	1.96	1.83	0.54	9.04	36.99
S25	1981.22	62.55	16.38	7.18	0.66	0	0.63	0	3.15	9.45
S26	2511.34	45.62	4.44	0.86	0	19.08	1.34	0.47	1.63	26.56
S27	1975.82	61.51	13.21	10.15	0.98	0	0.69	0	4.82	8.64
S28	2031.06	28.48	12.91	4.56	0.79	14.76	0	0.93	3.86	33.71
S29	2038.04	33.85	31.89	3.14	0.45	5.36	0	1.13	2.12	22.06
S30	2054.36	42.32	9.40	2.60	1.55	4.95	0	1.76	2.15	35.27
S31	1903.22	49.18	3.60	1.09	0.47	16.17	1.39	0	2.34	25.76
S32	1968.72	39.38	10.85	10.20	1.1	5.68	0	1.82	0.24	30.73
S33	1971.89	46.85	6.31	1.58	0.79	18.8	0	1.42	0.38	23.87
S34	1976.72	43.35	11.02	3.08	0.74	10.94	0	1.33	0.36	29.18
S35	1981.49	45.29	5.17	1.52	1.32	18	0	2.58	2.35	23.77
S36	1989.38	43.77	9.49	2.50	0	8.15	0	2.49	0.29	33.31
S37	1997.39	41.86	13.08	2.84	0.92	10.14	0	0.78	0.49	29.89
S38	2001.09	35.50	14.00	3.07	0	7.54	0	0.51	0.51	38.87

Zeiss Axioskop 40 fluorescence microscope to calculate the type index (TI) value. The TI value was calculated with reference to Ma et al., 2022.[52] 10 mg of isolated kerogen was combusted in a sampling device to obtain CO_2, and then the purified CO_2 was introduced into a MAT 253 gas stable isotope mass spectrometer for kerogen carbon isotope analysis ($\delta^{13}C_{kerogen}$), and the $\delta^{13}C_{kerogen}$ results were analyzed using the PDB standard.

The pyrite sulfur from samples was extracted following the method of "chromium reduction" by Canfield et al., 1986.[53] Approximately 5 g of sample was extracted with dichloromethane for 24 h to remove organic matter and elemental sulfur, and then the sample was dried, and 6 mol/L HCl was added to remove carbonates and acid-volatile monosulfides. Subsequently, a mixture of 15 mL of 12 mol/L HCl and 15 mL of 1 M $CrCl_3$ was added to the sample for 2 h under N_2 flow to produce H_2S, while a silver nitrate ($AgNO_3$) trap was attached to react H_2S with $AgNO_3$ to obtain precipitate silver sulfide. Finally, the solution was filtered through a 25 mm filter, and the precipitate was dried in a drying oven. The results of pyrite

sulfur isotopes ($\delta^{34}S_{py}$) were tested by a Delta V Advantage isotope ratio mass spectrometer according to the Canyon Diablo Troilite (V-CDT) standard, and sulfur isotope reference materials IAEA-S-1 (−0.3‰) were measured.

4. RESULTS

4.1. Morphology and Characteristics of Pyrite. Pyrite is abundant throughout the black shales of the Chang 7 Member of the Ordos Basin. Microscopically, the pyrite types mainly included framboidal, spherulitic, euhedral, and anhedral pyrite and their aggregates (Figure 2). Many intercrystalline and dissolution pores were developed in framboidal and spherulitic pyrites and their mineral aggregates.

4.1.1. Framboidal Pyrite (Type A). Framboidal pyrite is an aggregate composed of pyrite microcrystals that are generally polygonal or octahedral with a uniform particle size and filled with organic matter (Figure 2A). Framboidal pyrite formed by a series of chemical reactions and polymerization under magnetic force when the concentration of in situ active iron in sulfur-containing water was high.[15] The shape and crystal size

were used to determine the formation environment and stage of the framboidal pyrite.[54] During the syn-depositional period, pyrite was precipitated from sulfur-containing anoxic water bodies and rapidly settled on the surface of sediments due to gravity.[55] As a result, pyrite growth was affected by the growth time and available space, and the particle size was mostly limited to less than 5 μm.[49,57] The early diagenetic stage pyrites mainly crystallized in the sediment pores below the redox interface. The particle size was mainly between 5 and 10 μm, with some exceeding 10 μm.[18] The size of the framboidal pyrite aggregates in the Chang 7 Member exceeded 10 μm (Figure 2A,C), which showed that the framboidal pyrite formed during the syn-sedimentary to early diagenetic stage. Moreover, many intercrystalline pores developed in the framboidal pyrite aggregates and were surrounded and filled with liquid hydrocarbons (Figure 2C).

4.1.2. Spherulitic Pyrite (Type B). Spherulitic pyrites are mostly irregular shapes, usually formed by the early formation of framboidal pyrites recrystallized by later diagenesis and combined under the close aggregation of grains. These framboidal pyrite aggregates were pressurized during the rock layer compaction. The mutual extrusion of pyrite crystals changed the shape of the internal pyrite crystals, creating a spherulitic or an ellipsoidal shape.[18] The outline of the early framboidal pyrite aggregates remained at the edge of the spherulitic pyrite in the study samples, and the particle size was similar to that of framboidal pyrite (Figure 2B). The continuous growth of spherulitic pyrite during diagenesis led to extrusion deformation of the clay-organic matter layer on the upper and lower sides of the crystal, and cracks developed inside.

In contrast, diagenesis did not significantly affect the crystal form of the upper euhedral pyrite. These phenomena show that the formation time of spherulitic pyrite was later than that of framboidal pyrite and earlier than that of euhedral pyrite. In addition, there were distinct dissolution pores in the spherulitic crystals, and the liquid hydrocarbon ring was observed under an environmental scanning electron microscope, showing shale oil residues (Figure 2B).

4.1.3. Euhedral and Anhedral Pyrites (Type C). Euhedral pyrite forms include octahedra and cubes and appeared as isolated crystals and their aggregates, often euhedral or semieuhedral crystals. Euhedral pyrite with large particle size variations typically coexists with clay particles or lamellae. The pyrite particles between the clay lamellae are typically surrounded by organic matter. Euhedral pyrite aggregates were often present near organic matter or marginal cracks (Figure 2D,E). This type of pyrite usually formed during the diagnostic stage when the rock pores were relatively closed. Sulfur-containing water was retained, and the material supply for pyrite formation was insufficient. This was mainly based on the growth of pyrite crystallites, which finally formed euhedral pyrite crystals. During crystal growth, the degree of saturation of the solution determined the crystal morphology of pyrite. The appearance of euhedral crystals indicated a long period of low saturation sulfur concentrations in the sedimentary environment.[18] SEM showed that the euhedral pyrite was mostly in mosaic in contact with organic matter and clay minerals and developed intercrystalline pores, which were conducive to the retention of liquid hydrocarbons generated by organic matter in the later period (Figure 2D).

Compared to framboidal pyrite, anhedral pyrite crystals and their aggregates were usually irregular monomer particles or irregular aggregate masses and often coexisted with clay minerals. The SEM showed that the allomorph pyrite mostly filled in shale cracks and clay minerals (Figure 2F), supporting diagenesis and preserving certain reservoir spaces. This phenomenon was conducive to the filling and maintaining of oil and gas generated by organic matter in the later stage.

4.2. Mineral Composition. The results of XRD analysis of the original shale samples are listed in Table 1 and are shown in Figure 3. The mineral compositions of different samples
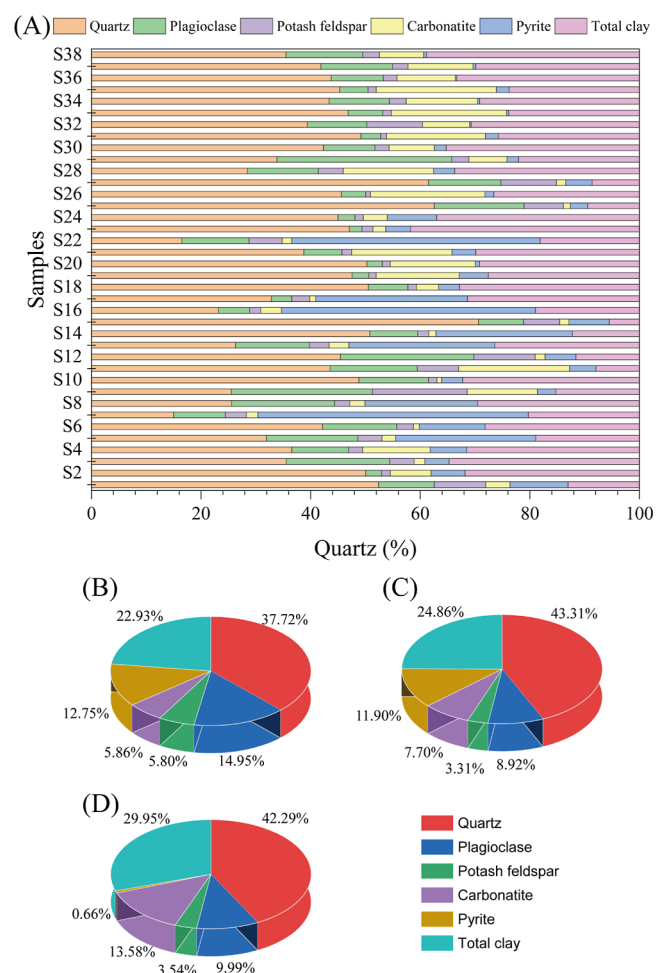

Figure 3. (A) Mineral composition of Chang 7 shale; (B) type A pyrite; (C) type B pyrite; (D) type C pyrite.

showed strong heterogeneity, with quartz and clay being the dominant minerals (Figure 3A). The quartz content was between 14.97 and 70.64%, with an average of 41.35%, and the clay mineral content was between 5.52 and 41.77%, with an average of 25.19%. The feldspars in the samples were mainly plagioclase and potash, with average contents of 11.02 and 4.14%, respectively. The distribution of carbonate minerals (predominantly calcite and dolomite) was highly uneven, with carbonate contents ranging from 0.85 to 21.90%, with an average of 8.21%. Pyrite was the main authigenic metal sulfide in the study area. The pyrite contents were between 0.24 and 49.33%, with an average of 10.10%. However, the pyrite contents in types A, B, and C showed distinct differences, with average contents of 12.75, 11.90, and 0.66%, respectively (Figure 2B−D).

Table 2. TOC, TS, $\delta^{34}S_{py}$, $\delta^{13}C_{kerogen}$, and Kerogen type Shale Samples from the Chang 7 Member

samples	depth/m	TOC/%	TS/%	kerogen macerals/%						$\delta^{13}C_{kerogen}$/‰	$\delta^{34}S_{py}$/‰
				sapropelic	exinite	vitrinite	inertinite	TI	kerogen types		
S1	2035.42	10.27	3.92	90.4	0.1	8.9	0.6	83.18	I	−30.22	−4.206
S2	1910.23	7.15	2.48	87.7	2.8	9.2	0.4	81.78	I	−32.35	−3.815
S3	2044.06	7.44	2.62	93.3	0	4.2	2.5	87.65	I	−31.57	−4.337
S4	2048.12	9.59	3.61	97.5	0	1.6	0.9	95.40	I	−32.9	−2.159
S5	2058.31	11.31	4.41	94.0	0	5.0	1.0	89.25	I	−32.33	−3.168
S6	2060.26	8.29	3.01	96.0	0	3.6	0.4	92.90	I	−30.63	−0.987
S7	2071.82	19.75	8.32	98.1	0	1.9	0	96.67	I	−34.43	−1.265
S8	2079.38	10.72	4.14	96.7	0	3.3	0	94.23	I	−32.98	−2.158
S9	2080.26	7.36	2.59	93.9	0	5.1	1.0	89.08	I	−30.9	−1.034
S10	1984.13	4.71	1.36	89.5	4.7	5.7	0	87.59	I	−29.7	−0.766
S11	1967.29	5.43	1.69	93.8	0.7	5.5	0	89.99	I	−30.66	−2.114
S12	1969.52	5.21	1.58	88.4	2.2	9.3	0	82.55	I	−30.42	−2.857
S13	2005.16	10.82	4.18	86.6	0.2	12.4	0.8	76.60	II$_1$	−30.42	0.203
S14	2006.08	9.47	3.56	82.4	0.1	16.7	0.8	69.13	II$_1$	−28.78	0.487
S15	2007.22	7.46	2.63	85	0.2	14.2	0.6	73.85	II$_1$	−28.88	1.269
S16	2034.48	17.07	7.07	84.4	0.1	14.5	1.0	72.58	II$_1$	−29.27	2.113
S17	2041.22	12.01	4.73	84.2	0.2	14.6	1.0	72.35	II$_1$	−28.42	2.967
S18	1986.15	6.74	2.29	78.6	4.5	16.9	0.1	68.05	II$_1$	−27.16	0.982
S19	1972.39	6.58	2.26	70.7	2.6	26.5	0.2	51.96	II$_1$	−28.68	3.163
S20	2507.37	3.21	0.68	74.7	1.2	24.0	0.1	57.19	II$_1$	−28.32	2.697
S21	1965.66	3.26	0.74	86.1	0.3	13.5	0.1	76.03	II$_1$	−29.76	2.367
S22	2067.61	13.59	5.52	81.6	0	18.4	0	67.80	II$_1$	−28.36	3.052
S23	1977.48	5.82	1.92	75.6	1.3	22.2	0.9	58.76	II$_1$	−29.29	3.144
S24	1980.96	7.8	2.81	87.1	1.4	11.6	0	79.04	II$_1$	−29.06	1.633
S25	1981.22	4.16	1.13	87.7	0.9	11.4	0	79.61	II$_1$	−29.56	1.534
S26	2511.34	2.66	0.42	85.1	0.4	14.5	0	74.41	II$_1$	−28.83	1.489
S27	1975.82	5.07	1.53	78.8	4.2	16.9	0	68.24	II$_1$	−28.62	2.016
S28	2031.06	3.08	0.61	57.9	0	37.7	4.4	25.23	II$_2$	−27.35	4.596
S29	2038.04	2.57	0.38	54.7	0	45.3	0	20.73	II$_2$	−27.7	5.012
S30	2054.36	1.14	0.12	46.0	0	51.0	3.0	4.75	II$_2$	−27.24	5.113
S31	1903.22	3.37	0.66	51.3	5.4	43.0	0.34	21.39	II$_2$	−29.58	3.986
S32	1968.72	2.05	0.21	1.0	1.0	96.0	2.0	−72.50	III	−26.33	8.984
S33	1971.89	0.84	0.16	1.9	1.5	95.2	1.4	−70.15	III	−26.25	6.772
S34	1976.72	1.48	0.23	15.5	0.1	82.7	1.7	−48.17	III	−28.38	5.772
S35	1981.49	1.15	0.11	7.5	0.1	86.2	6.3	−63.31	III	−27.39	9.136
S36	1989.38	0.61	0.23	14.9	6.0	76.0	3.1	−42.20	III	−25.33	6.135
S37	1997.39	0.64	0.19	0	6.2	93.6	0.2	−67.30	III	−25.06	8.383
S38	2001.09	0.77	0.25	0	16.7	82.3	1.0	−54.38	III	−26.42	7.229

4.3. Geochemical Characteristics.

4.3.1. TOC and TS Concentrations.

The geochemical characteristics (TOC, TS, $\delta^{34}S_{py}$, $\delta^{13}C_{kerogen}$, and kerogen types) of 38 samples are listed in Table 2. The TOC content was between 0.61 and 19.75 wt %, with an average of 6.33 wt %, and the TS content was between 0.11 and 8.32 wt %, with an average of 2.22 wt %. The TOC and TS contents of the samples with type A pyrite were the highest, ranging from 4.71 to 19.75 wt % (with an average of 8.94 wt %) and 1.36 to 8.32 wt % (with an average of 3.31 wt %), respectively. The TOC and TS contents of the samples with type B pyrite ranged from 1.14 to 17.07 wt % (with an average of 6.63 wt %) and from 0.12 to 7.07 wt % (with an average of 2.28 wt %), respectively. The TOC and TS contents of the samples with type C pyrite ranged from 0.61 to 2.05 wt % (with an average of 1.08 wt %) and from 0.11 to 0.25 wt % (with an average of 0.20 wt %), respectively.

4.3.2. Types and Carbon Isotope Characteristics of Kerogen.

Based on the kerogen macerals and TI (Table 2), the kerogen types in the source rocks of the Chang 7 Member of the Central Ordos Basin display heterogeneity (Figure 4).
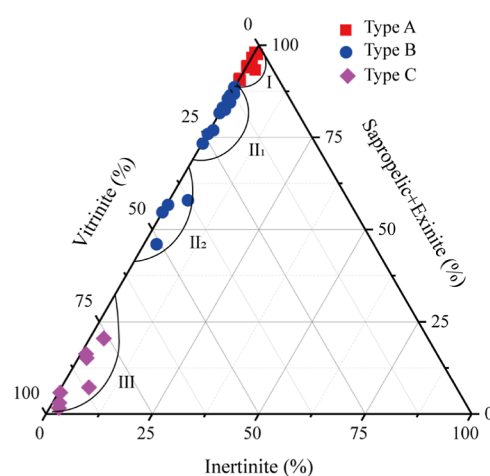

Figure 4. Kerogen types with different pyrites in the Chang 7 shale of the Central Ordos Basin.

Type I kerogen (TI > 80) accounted for 31.56% of all samples. In contrast, type II$_1$ kerogen (TI = 40−80) accounted for 39.47% of the total sample. Type II$_2$ kerogen (TI = 0−40) accounted for 10.53% of all samples. Type III kerogen (TI < 0) accounted for 18.42% of all samples. The statistical results from the FE-SEM and kerogen TI analyses indicated that the main pyrite types associated with type I, II, and III kerogens were classified as type A, type B, and type C, respectively.

Significant differences were observed according to the distribution of kerogen carbon isotopes ($\delta^{13}C_{kerogen}$) in different pyrite samples (Figure 5 and Table 2). Specifically,
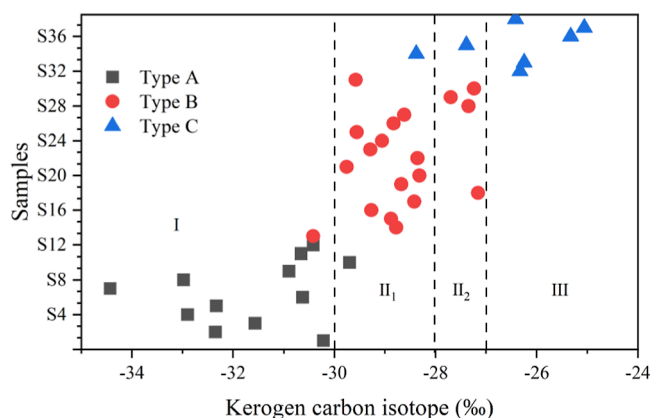
Figure 5. Kerogen carbon isotope value divides the organic matter type with different pyrites.

the $\delta^{13}C_{kerogen}$ values in the samples with type A pyrite are the lightest, ranging from −34.43 to −29.70‰ (with an average of −31.59‰). For samples with type B and type C pyrite, the $\delta^{13}C_{kerogen}$ values gradually become heavier, with distributions of −30.42 to −27.16‰ (with an average of −28.70‰) and −28.38 to −25.06‰ (with an average of −26.45‰), respectively.

4.3.3. Sulfur Isotopic Compositions of Pyrites ($\delta^{34}S_{py}$). The distribution of sulfur isotopes in the Chang 7 Member shale samples in the Ordos Basin showed strong heterogeneity, with

values ranging from −5.265 to 9.136‰ (with an average of 1.615‰). However, the $\delta^{34}S_{py}$ values in shale samples with different pyrite types showed a reasonable regularity (Figure 6). The $\delta^{34}S_{py}$ values in shale with type A pyrite were the lightest, ranging from −5.265 to −0.766‰ (with an average of −2.739‰). The $\delta^{34}S_{py}$ values in shale with type B and type C pyrite ranged from 0.113 to 5.113‰ (with an average of 2.201‰) and from 5.772 to 9.136‰ (with an average of 7.487‰), respectively. The results showed a gradual increase in sulfur isotope ratios in type A, B, and C pyrites.

4.4. Distribution Characteristics of Shale Oil. *4.4.1. Rock-Eval Pyrolysis.* The Rock-Eval pyrolysis results for the original shale samples are presented in Table 3 and Figure 6. The T_{max} of shale samples ranged from 440 to 463 °C (with a mean value of 451 °C), indicating the shale samples were in the low maturity to maturity stages.[46] In shales with types A, B, and C pyrites, the T_{max} ranged 440−461 °C (average, 449 °C), 441−463 °C (average, 449 °C), and 454−460 °C (average, 447 °C), respectively, with no significant difference overall. S_1 is an index of the free oil content of residual oil in the shale. The S_1 values for shale samples ranged from 0.09 to 4.87 mg/g (with a mean value of 1.80 mg/g), and the S_1 values in the shales with pyrite types A, B, and C were 1.32−3.87 mg/g (average, 2.38 mg/g), 0.12−4.87 mg/g (average, 1.90 mg/g), and 0.09−2.02 mg/g (average, 0.55 mg/g), respectively. S_2 is an index of the adsorbed residual oil content in the shale. The S_2 of shale samples ranged from 0.53 to 57.28 mg/g (with a mean value of 18.06 mg/g), and the S_2 values in shales with types A, B, and C pyrites were 6.22−57.28 mg/g (average, 23.26 mg/g), 0.53−55.66 mg/g (average, 20.73 mg/g), and 0.54−6.55 mg/g (average, 1.92 mg/g), respectively. The TOC and pyrolysis data showed that the samples of the Chang 7 Member contained a complex petroleum potential but showed distinct regularity with the type of pyrite (Figure 7A). In addition, most samples with type A pyrite contained good to excellent petroleum potential, but the petroleum potential of shale with type B pyrite was medium to poor. The petroleum potential of shale with type C pyrite was poor and the lowest among all of the shales. The organic matter maturity was characterized based on the PI
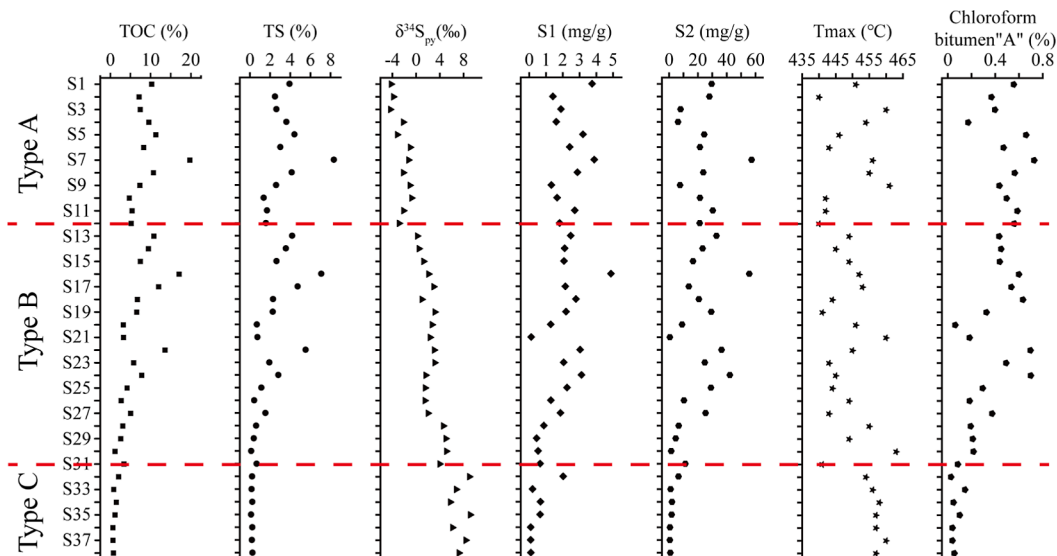

Figure 6. Profiles for TOC, TS, $\delta^{34}S_{py}$, Rock-Eval pyrolysis, and chloroform bitumen "A" of the Chang 7 Shale. The red dashed lines represent the boundary that separates different pyrite development horizons.

Table 3. Rock-Eval Pyrolysis and Chloroform Bitumen "A" Content of the Chang 7 Member Shale Samples

samples	depth (m)	Rock-Eval pyrolysis			chloroform bitumen "A"/%				
		S_1/%	S_2/%	T_{max}/°C	content	saturate	aromatic	resin	asphaltene
S1	2035.42	3.74	29.54	451	0.5553	49.69	19.02	23.31	7.98
S2	1910.23	1.41	27.99	440	0.3676	34.65	21.05	23.24	21.06
S3	2044.06	1.89	7.97	460	0.3970	20.33	20.33	21.31	38.03
S4	2048.12	1.61	6.22	454	0.1708	42.76	22.49	20.93	13.82
S5	2058.31	3.2	24.38	446	0.6593	54.26	17.05	13.93	14.76
S6	2060.26	2.41	21.41	443	0.4697	47.37	22.10	22.11	8.42
S7	2071.82	3.87	57.28	456	0.7275	67.30	16.34	12.27	4.09
S8	2079.38	2.87	23.74	455	0.5635	52.57	19.24	16.56	11.63
S9	2080.26	1.32	7.61	461	0.4345	41.36	24.82	17.28	16.54
S10	1984.13	1.66	21.43	442	0.4950	24.92	8.72	37.69	28.67
S11	1967.29	2.71	30.33	442	0.5862	41.72	16.00	25.71	16.57
S12	1969.52	1.81	21.25	440	0.5611	45.94	17.30	24.87	11.89
S13	2005.16	2.47	32.90	449	0.4323	45.16	18.82	19.89	16.13
S14	2006.08	2.11	23.29	445	0.4490	51.34	21.39	26.20	1.07
S15	2007.22	2.07	16.62	449	0.4373	50.28	24.31	19.33	6.08
S16	2034.48	4.87	55.66	452	0.5987	56.89	13.77	22.75	6.59
S17	2041.22	2.15	13.71	453	0.5353	56.19	17.78	16.51	9.52
S18	1986.15	2.78	20.69	444	0.6331	11.68	20.80	15.69	51.83
S19	1972.39	2.19	29.26	441	0.3254	16.02	26.93	14.42	42.63
S20	2507.37	1.28	9.02	451	0.0621	11.24	20.85	10.54	57.37
S21	1965.66	0.12	0.53	460	0.1830	34.24	18.50	28.76	18.50
S22	2067.61	3.03	36.42	450	0.6963	52.36	15.86	24.13	7.65
S23	1977.48	2.05	24.8	443	0.4914	31.22	23.70	24.85	20.23
S24	1980.96	3.11	42.18	445	0.6992	45.81	21.93	19.36	12.90
S25	1981.22	2.25	29.04	444	0.2934	18.06	27.76	15.37	38.81
S26	2511.34	1.29	10.32	449	0.1832	19.51	14.64	18.90	46.95
S27	1975.82	1.86	25.33	443	0.3732	24.72	22.47	39.33	13.48
S28	2031.06	0.87	6.69	455	0.1922	19.30	16.72	16.40	47.58
S29	2038.04	0.44	4.61	449	0.2100	19.93	19.20	17.39	43.48
S30	2054.36	0.53	1.49	463	0.2164	21.62	20.72	20.72	36.94
S31	1903.22	0.65	11.28	441	0.0839	16.62	24.30	13.55	45.53
S32	1968.72	2.02	6.55	454	0.0262	11.19	22.03	16.43	50.35
S33	1971.89	0.2	1.07	456	0.1443	16.90	28.26	17.45	37.39
S34	1976.72	0.67	2.03	458	0.0478	13.24	13.91	25.16	47.69
S35	1981.49	0.65	1.78	457	0.0998	17.65	23.23	15.88	43.24
S36	1989.38	0.09	0.61	457	0.0384	13.17	17.87	12.54	56.42
S37	1997.39	0.09	0.54	460	0.0380	18.28	21.14	24.57	36.01
S38	2001.09	0.1	0.86	457	0.0546	18.22	22.85	17.86	41.07

versus T_{max} value plot (Figure 7B), as given by Peters and Cassa (1994),[56,57] which shows that the Chang 7 Member shale samples were within the oil window zone.

4.4.2. Characteristics of Chloroform Bitumen "A". The chloroform bitumen "A" results for the original shale samples are listed in Table 3 and Figure 6. The chloroform bitumen "A" of shale samples ranged from 0.0262 to 0.7275% (mean value, 0.3561%), showing that the shale samples had good oiliness. The shale with type A pyrite had the best oil-bearing property, with the chloroform bitumen "A" content distributed in the range of 0.1708−0.7275% (average, 0.4990%). In contrast, the chloroform bitumen "A" in type B and type C pyrite was in the range 0.0621−0.6992% (average, 0.3734%) and 0.0262−0.1443% (average, 0.0642%), respectively. Generally, the chloroform bitumen "A" oil components extracted from shale samples or crude oils mainly include saturate, aromatic, resin, and asphaltene (SARA), and different proportions reflect the physical properties of organic hydrocarbons. The content of saturated hydrocarbon components in the chloroform bitumen "A" composition in Chang 7 shale was high, ranging from

11.19 to 67.30% (average, 32.47%), followed by asphaltene content ranging from 1.07 to 57.37% (average, 27.08%). The aromatic and resin contents were low, with averages of 20.11 and 20.35%, respectively, but the saturate/aromatic values were high, ranging from 0.51 to 4.13 (average of 1.73). Table 3 shows the differences in group components in shale with different pyrite types and that samples with type A pyrite had the highest saturation content (average of 43.57%), the lowest asphaltene content (average of 16.12%), and the best fluidity.

5. DISCUSSION

5.1. Relationship between Pyrite Types and Organic Matter Enrichment. The sulfur isotope ($\delta^{34}S$) values of different types of pyrite are significantly different.[58] The $\delta^{34}S$ of syn-sedimentary pyrite generally shows negative values, while that of overgrown framboidal pyrite shows positive values and the positive anomalies of $\delta^{34}S$ of euhedral pyrite are more prominent. The mean sulfur isotope values of types A, B, and C pyrite show a tendency to increase sequentially (the mean values are −2.739, 0.113, and 5.113‰, respectively),
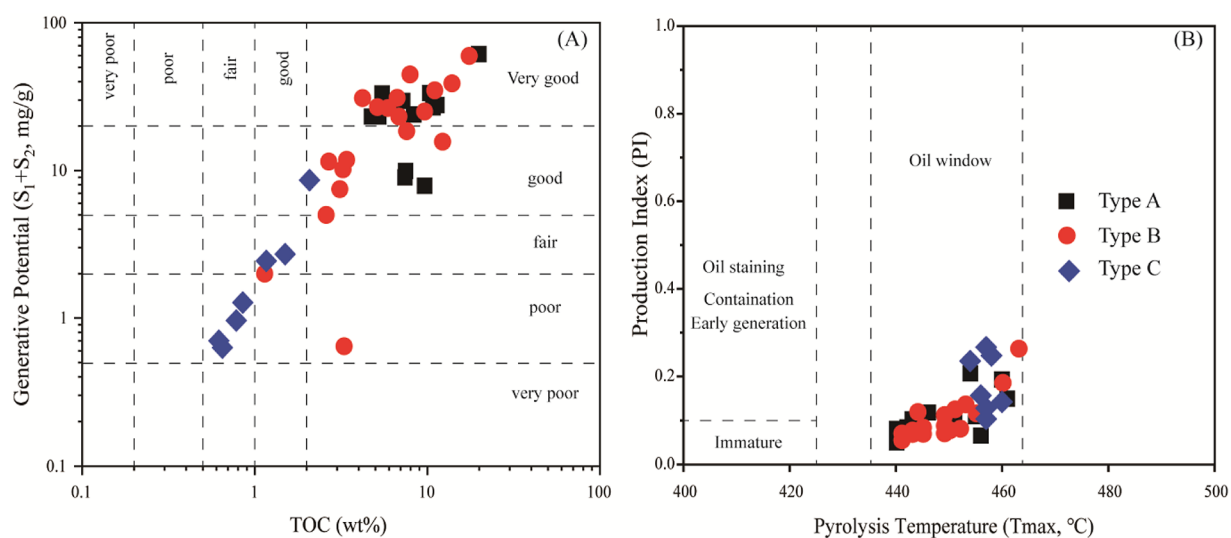
Figure 7. Plot of (A) generative potential ($S_1 + S_2$) vs TOC content; (B) T_{max} vs production index of Chang 7 Member shale samples, modified later (Liu et al., 2022).
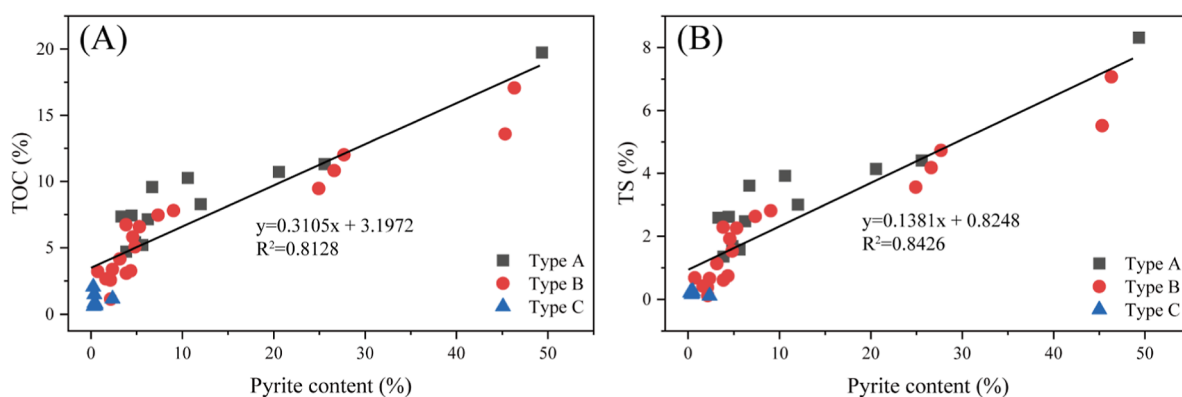

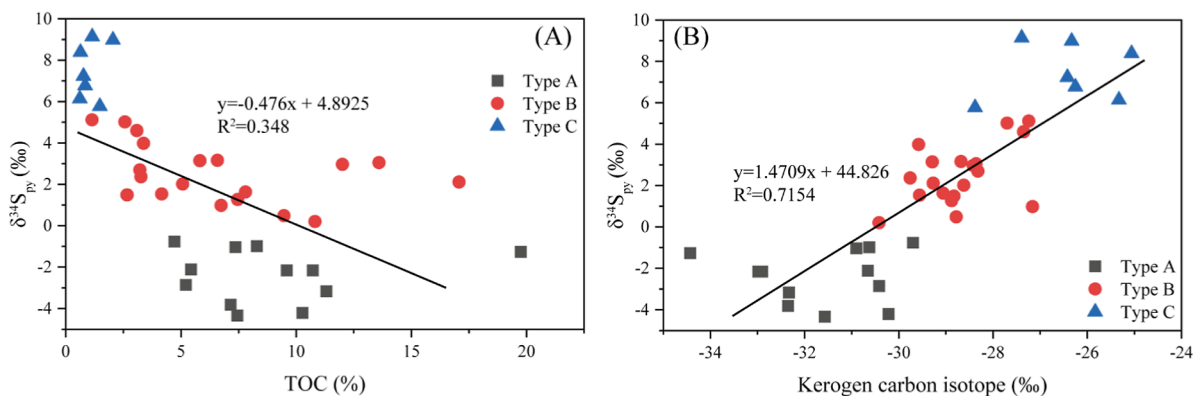**Figure 8.** Relationship between the pyrite content, TOC (A), and TS (B) of different pyrite types.

Figure 9. Relationship between TOC (A) and the kerogen carbon isotope (B) with sulfur isotopic compositions of pyrites ($\delta^{34}S_{py}$) of different pyrite types.

indicating that type A pyrite was formed during the syn-sedimentary to early diagenetic stage. In contrast, types B and C pyrite were formed during the early and middle diagenetic stages.

The formation of pyrite is controlled by the supply of sulfate in water, the organic matter input, and the active iron content.[59,60] Berner (1970) believed that in a typical shallow sea environment, the terrestrial supply provided sufficient active iron, and the sulfate content of seawater was also enough.[61] However, owing to water oxidation and the poor preservation conditions of organic matter, the input of organic matter determines the pyrite content.[62] Therefore, there is a high correlation between organic carbon and pyrite content.[63] Analysis of the TOC, TS, and XRD data of the Chang 7 black shales showed that there was a significant positive correlation between the pyrite content and the TOC content (Figure 8A),

as well as between TS and pyrite content (Figure 8B), indicating a coupled relationship between pyrite and organic matter.

The pyrite type in studied samples is mainly framboidal pyrite (type A) formed in the syn-sedimentary stage and spherulitic pyrite (type B) formed in the early diagenetic stage. Type A and type B pyrite contents significantly correlated with the TOC content (Figure 8A), indicating that framboidal pyrite and spherulitic pyrite are strongly associated with organic matter enrichment. However, there was no correlation between the type C pyrite content formed in the middle diagenetic stage and the TOC and TS. The SEM analysis indicated abundant organic matter in the periphery and intercrystalline pores of type A and type B pyrite, whereas clay minerals dominated type C pyrite. This phenomenon showed that only type A and B pyrites are strongly associated with organic matter enrichment, which was related to the positive charge of iron (pyrite colloids) in water and the negatively charged organic matter aggregate. Charge neutralization and flocculation often occurred between the two, forming organic metal complexes that coprecipitated. The initial formation of ferrous sulfide microcrystals often occurs on the surface of organic matter. Therefore, the initial growth basis of pyrite was located on the surface of organic matter and gradually transformed into type A pyrite in a suitable sedimentary environment in a later stage. This result was also confirmed by the intercrystalline pores of framboidal pyrite containing abundant organic matter (Figure 2A,C).

Figure 9A reveals a negative correlation between the TOC and sulfur isotopes of pyrite; however, there was no correlation between the TOC and sulfur isotope values of different pyrite types. The weak correlations between the isotopic composition of the sulfur in pyrite and TOC indicated that TOC was not the main factor controlling the differences in pyrite types in the Chang 7 Member of the Ordos Basin. However, there was a positive correlation between kerogen carbon isotopes and pyrite sulfur isotopes (Figure 9B), without a correlation between kerogen carbon isotopes and different pyrite types, which also confirms that TOC is not a significant factor controlling the differences in pyrite types and the organic matter type is an important influencing factor. Since organic matter type is correlated with the sulfur content, this also indicated that the sufficient sulfate supply required for pyrite formation during the depositional period of the Chang 7 Member was the main reason for the abnormal development of pyrite. The lake basin likely had a higher sulfate content than the standard freshwater lake basin during the deposition period of the Chang 7 Member. The sulfate source may be related to transgression, lake hydrothermal fluid, volcanic eruption, and other possible sources.[47]

5.2. Indicative Significance of Pyrite Type to Organic Matter Type.
Previous research has confirmed that framboidal pyrite is mainly developed in organic-rich shale with better organic matter types, but the potential correspondence between other pyrite and organic matter types is unknown.[49] The results of kerogen TI and the observation of pyrite morphology under SEM showed that the type I kerogen development layer was mainly enriched in framboidal pyrite (type A); the type II kerogen development layer was mainly enriched in spherulitic pyrite (type B); and the type III kerogen development layer was mainly enriched in euhedral and anhedral pyrites (type C). These results preliminarily confirmed the correspondence between the

types of organic matter and pyrite. The correlation analysis displayed a negative correlation between $\delta^{34}S_{py}$ and TI (Figure 10). With the $\delta^{34}S_{py}$ values ranging from negative to positive,

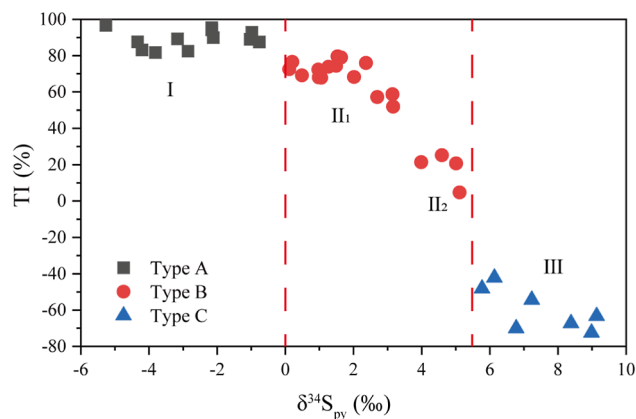**Figure 10.** Relationship between sulfur isotopic compositions of pyrites ($\delta^{34}S_{py}$) and the kerogen TI of different pyrite types. The red dashed lines represent the boundaries of sulfur isotope differences between different types of pyrite.

the kerogen type gradually changed from type I to type III and had distinct zoning, which indicated that different pyrite types could identify the type of organic matter. Sapropelic organic matter is mainly derived from plankton, benthos, and aquatic plants in water.[52] The formation and stagnant basin conditions usually reduced the environment. In this stage, pyrite preferentially crystallized into framboidal pyrite after precipitation from sulfur-containing water and anoxic water. It displayed the characteristics of bedding distribution with organic matter.[15,18] As the diagenetic process progresses, these framboidal pyrite aggregates are compressed during the compaction of the rock layer (Figure 2B). The mutual extrusion of pyrite crystals caused the shape of the internal pyrite crystals to change, showing spherical or oval shapes. Humic organic matter mainly originates from higher plants and is primarily formed in weak oxidation—oxidation environments. During this stage, organic matter functioned as a reducing agent to form FeS and then formed pyrite in different ways, which consumed organic matter. These results accounted for the low TOC content in type C pyrite. In addition, the diagenetic environment was not conducive to excessive pyrite formation, which was directly precipitated only in the sulfur-containing water of the shale pores. This result also accounted for the low pyrite content in type III organic matter shales. There was no correlation between the type C pyrite content and the TOC (Figure 8A). Thus, the development of type A and B pyrites indicates type I—II organic matter, whereas the development of type C pyrite indicates type III organic matter.

5.3. Indicative Significance of Pyrite Type to the Differential Enrichment of Shale Oil.
5.3.1. Pyrite vs Rock-Eval Pyrolysis. Figure 11 shows the relationship between the pyrite type, free hydrocarbons (S_1), and pyrolyzed hydrocarbons (S_2) in the organic-rich shale. Figure 11A shows a significant positive correlation between the pyrite content and S_1, and there is a distinct two-stage feature at 15% pyrite content. When the pyrite content exceeded 15%, the pyrite types in the shale were mainly type A and type B, with a positive correlation between these two pyrite types and S_1.
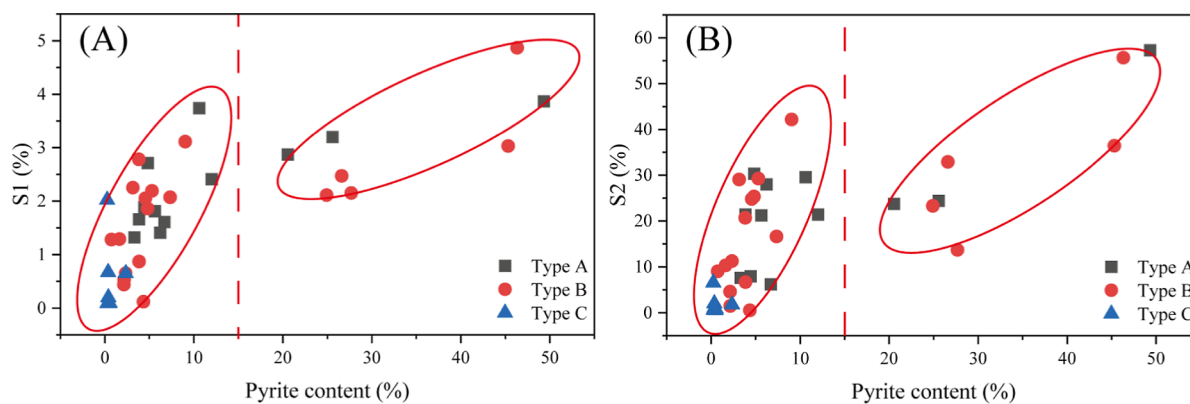
Figure 11. Relationship between S_1 (A), S_2 (B), and pyrite contents of different pyrite types. The red dashed lines represent the boundaries at 15% pyrite content.

When the pyrite content was less than 15%, the positive correlation between pyrolysis S_1 and type A and B pyrite was substantial; however, there was no correlation with type C pyrite. This phenomenon indicated that type A pyrite mainly formed in the syn-sedimentary period and type B pyrite formed in the early diagenetic period were directly involved in the pyrolysis of organic matter and the hydrocarbon generation process. Type C pyrite formed during the middle diagenetic period may have played a relatively limited role in pyrolysis and hydrocarbon generation processes for organic matter. The pyrite formed in the syngenetic period accumulates and nucleates in a dispersed form under magnetic force, gradually forming a complete type A pyrite. The large number of intergranular and intergranular pores developed in these pyrites can provide a place to enrich liquid hydrocarbons. Through SEM statistics, Guangrong et al. (2020) believed that the reservoir space supplied by type A pyrite can increase the porosity by about 2%.[18] On the one hand, the intergranular and intercrystalline pores of the early formed framboidal pyrite are destroyed due to the dissolution of organic acid, which inhibits the development of pores. On the other hand, developing dissolution pores in type B pyrite can also provide some reservoir space for liquid hydrocarbons. Type C pyrites are primarily formed in the late stage of early diagenesis to the early stage of middle diagenesis, and the pyrite particles have no noticeable pores under the microscope. However, pyrite is a vital skeleton mineral in shale, and its compressive solid strength can protect the original pores from being destroyed during compaction. Therefore, whatever type of pyrite is conducive to enriching liquid hydrocarbons.

Figure 11B shows that the pyrolyzed hydrocarbons (S_2) of the black shale in the Chang 7 Member of the Ordos Basin were between 0.53 and 57.28 mg/g, which were significantly higher than the content of free hydrocarbons (S_1). This phenomenon was due to the low maturity of the Chang 7 black shale (with R_o values between 0.7 and 1.1%) and the large amount of organic matter that had not yet been converted to oil and gas.[44,45] Similar to S_1, the pyrite content and S_2 also showed distinct two-stage characteristics (Figure 11B). When the pyrite content exceeded 15%, with an increase in the pyrolysis temperature, the liquid hydrocarbons generated during pyrolysis from type I and type II organic matter, as indicated by type A and type B pyrites, were significantly higher than those generated from type III organic matter, as indicated by type C pyrite. This phenomenon may involve the difference in the organic matter type or be affected by the

difference in the surface properties of different pyrite types. Therefore, further analysis of the content and composition of liquid hydrocarbons remaining in the shale reservoir space is necessary to determine the influence of the pyrite content and type on the shale oil enrichment process.

As a result, types A, B, and C pyrites are developed at pyrite contents below 15%, while types A and B pyrites are predominantly developed at pyrite contents above 15%, and higher types A and B pyrite contents are indicative of more excellent free and pyrolyzed hydrocarbon production. This phenomenon was related to the formation time of different pyrite types and the difference in the types of organic matter. Types A and B pyrites were formed earlier, with smaller grain sizes and the development of intercrystalline pores between the pyrite microcrystals (Figure 2C) and dissolution pores (Figure 2B), which provide reservoir space for hydrocarbons, such as the filling of organic matter around or inside the framboidal pyrite (Figure 2A,C), indicating that the pyrite formation time was earlier than the significant oil generation period of kerogen. In contrast, type C pyrite was formed later, with a larger grain size and less pore development, which provides a limited reservoir space for hydrocarbons (Figure 2E,F). Meanwhile, types A and B pyrites are the main pyrite types developed at a higher pyrite content (>15%), and their abundant presence can reduce the activation energy of organic matter cracking and thus advance hydrocarbon production.[42,43] In addition, as previously mentioned, types A and B pyrites indicate types I and II organic matter with a high hydrocarbon generation potential, and the liquid hydrocarbon content generated during the thermal evolution process was significantly higher than that of type III organic matter. Therefore, the higher the content of types A and B pyrites, the higher the S_1 and S_2 contents.

5.3.2. Pyrite vs Chloroform Bitumen "A". Pyrite in shale increases the rate of organic matter cracking into oil and gas, which has been confirmed in experiments.[42,43] Pyrite is a favorable hydrocarbon expulsion channel for shale oil and gas and a reservoir space for shale oil.[40] The correlation analysis between the pyrite content and chloroform bitumen "A" (Figure 12) showed that pyrite in shale promoted shale oil enrichment, and there was a distinct boundary when the pyrite content is 15%. When the pyrite content exceeded 15%, there was a significant positive correlation between the pyrite content dominated by types A and B pyrite and chloroform bitumen "A". When the pyrite content was less than 15%, there was also a significant positive correlation between the pyrite
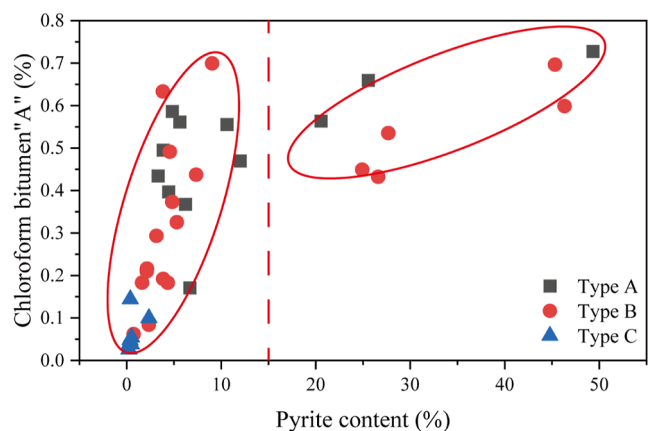
Figure 12. Relationship between the pyrite content and chloroform bitumen "A" of different pyrite types. The red dashed lines represent the boundaries at 15% pyrite content.

content and chloroform bitumen "A" as a whole, but there was no significant correlation between type C pyrite and chloroform bitumen "A". This phenomenon was related to the numerous nanoscale pores that developed between microcrystals in type A pyrite aggregates and numerous dissolution pores set in type B pyrite, which were conducive to the accumulation of liquid hydrocarbons. The abundant nanoscale pores provided a reservoir space for the enrichment of residual oil in shale, which was conducive to shale oil enrichment. There were distinct oil film phenomena in the intercrystalline and dissolution pores of types A and B pyrite particles under SEM, which also confirmed that these two pyrite types

promoted shale oil enrichment (Figure 2A−C). Thus, the higher content of types A and B pyrites is indicative of the greater soluble organic matter content in the Chang 7 Member shales.

However, type C pyrite lacks distinct crystal structures or dissolution pores. Consequently, type C pyrite did not directly contribute to the reservoir space for shale oil. Therefore, no significant correlation was observed between type C pyrite and chloroform bitumen "A". According to Guangrong et al. (2020), the source of type C pyrite was the sulfur-containing water from early liquid hydrocarbon generation in relatively closed clay mineral interlayers or fractures.[18] The formation time may occur later than the oil and gas filling times, which was also one of the reasons for the poor correlation between type C pyrite and residual oil in shale. However, a small amount of liquid hydrocarbon residue was also found in the euhedral pyrite aggregates of Chang 7 shale of the Ordos Basin (Figure 2D). Therefore, the formation time of type C pyrite may have been earlier than that of oil and gas filling; this pyrite was limited and did not play a leading role in shale oil enrichment and cannot be used as an indicator of shale oil enrichment.

5.3.3. Pyrite vs Oil Components. The relationships between pyrite type, contents, and components of extracts were analyzed to explore the role of pyrite in shale oil enrichment. Figure 13 shows that the pyrite content had a significant positive correlation with saturated hydrocarbons, no significant correlation with aromatics and resin, and a significant negative correlation with asphaltenes. Overall, this indicated that the abundance of pyrite was conducive to enriching light components and inhibiting the distribution of heavy
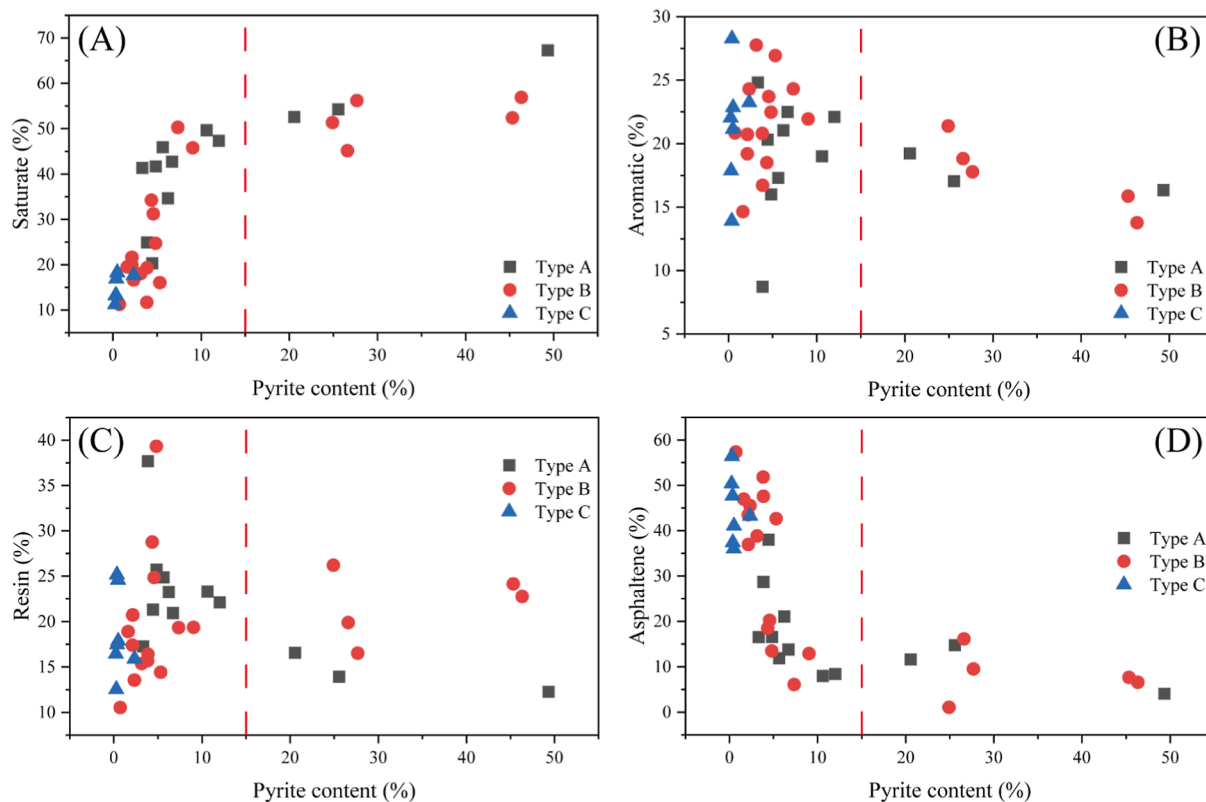

Figure 13. Relationship between pyrite content and oil components: (A) saturate; (B) aromatic; (C) resin; (D) asphaltene of different pyrite types. The red dashed lines represent the boundaries at 15% pyrite content.

components. This result was due to sulfur and Fe^{2+} that promoted pyrite formation during organic matter hydrocarbon generation, which reduced the activation energy required for organic matter cracking, promoted the hydrocarbon generation of organic matter, and discharged saturated hydrocarbons.[9] Specific analysis of this relationship revealed that different pyrite types and oil components exhibited distinct dual-stage distribution characteristics at 15% pyrite content.

When the pyrite content exceeded 15%, type A and type B pyrites showed a significant positive correlation with saturates (Figure 13A) and negative correlations with aromatics (Figure 13B), resin (Figure 13C), and asphaltene (Figure 13D), indicating that these two pyrite types promote the formation and enrichment of saturates and inhibit the enrichment of other components. This phenomenon was related to the efficiency of these two pyrite types in promoting the hydrocarbon generation of organic matter. Pyrite types are mainly types A and B at >15% pyrite content, as their high content catalyzes the hydrocarbon generation from organic matter cracking, resulting in the cracking of large molecular heavy hydrocarbons to generate light hydrocarbons. Moreover, pyrite can reduce the amount of aromatic polycyclic molecules by inhibiting aromatization, thus promoting the cracking of long-chain aliphatic hydrocarbons in kerogen to form relatively short-chain aliphatic hydrocarbons.[64] In addition, types I and II organic matter indicated by types A and B pyrites were conducive to the selective adsorption of heavy components. Due to the selective adsorption of heavy components, the saturates migrated to the intercrystalline in type A pyrite and the dissolution pores in type B pyrite because of their small molecular weight. Consequently, types A and B pyrites are positively correlated with saturates and negatively correlated with aromatics, resin, and asphaltene at >15% pyrite content.

When the pyrite content was less than 15%, types A and B pyrites showed a positive correlation with saturates and aromatics but a gradual negative correlation with resin and asphaltenes. This result indicated that types A and B pyrites were conducive to the enrichment of light components but inhibited the enrichment of heavy components. The underlying reasons for this included the early formation of types A and B pyrites and subsequent involvement in the catalytic pyrolysis and hydrocarbon generation. Inhibition of aromatization is reduced at <15% pyrite content, insufficient to cause a significant reduction in aromatic hydrocarbons. Thus, types A and B pyrites and aromatic hydrocarbons are positively correlated.

Furthermore, types A and B pyrites are mainly composed of intercrystalline and dissolved pores as the leading shale oil reservoir space, and the light components in the early generated liquid hydrocarbons easily migrate to these pores with relatively small molecular weights. In addition, types A and B pyrites indicated high-quality organic matter, which exhibited stronger selective adsorption to light components in shale oil during hydrocarbon generation than type C pyrite. Consequently, types A and B pyrites are positively correlated with saturates and aromatics and negatively correlated with other fractions at <15% pyrite content.

There was no correlation between type C pyrite and shale oil group components, which was related to the late formation time of type C pyrite and the limited liquid hydrocarbon reservoir space provided by type C pyrite. In addition, the organic matter type indicated by type C pyrite was mainly gas-prone type III, which was not conducive to forming liquid hydrocarbons. Thus, the development of types A and B pyrites is indicative of the enrichment of saturated and aromatic hydrocarbons at <15% pyrite content, whereas the development of types A and B pyrites is indicative of the enrichment of saturated hydrocarbons at >15% pyrite content. The development of types C pyrite is not indicative of shale oil enrichment.

6. CONCLUSIONS

Through systematic petrological and organic geochemical analyses, this study characterized pyrites in lacustrine shale and their implications for the differential enrichment of organic matter and shale oil. The results are as follows:

As the dominant authigenic metal sulfide in the Chang 7 shale, the pyrite content ranged from 0.24 to 49.33% (average of 10.10%). Three morphological pyrite types were observed: framboidal (type A), spherulitic (type B), and euhedral and anhedral (type C). The $\delta^{34}S$ values of type A pyrite are the lowest, ranging from −5.265 to −0.766‰ (average −2.739‰), indicating that type A pyrite likely formed during the syn-sedimentary to early diagenesis stage. The $\delta^{34}S$ values of type B and type C pyrites are relatively heavier, ranging from 0.113 to 5.113‰ (2.201‰) and from 5.772 to 9.136‰ (7.487‰), respectively, suggesting their formation during the early and middle diagenesis stages.

The intervals in which different pyrite types were enriched in the samples from the Chang 7 Member were closely related to the abundance and type of organic matter. The intervals where type A and type B pyrites developed had high TOC and TS contents. In addition, the leading organic matter types corresponding to the intervals with types A, B, and C pyrites were types I, II, and III, respectively.

The Chang 7 shale in the Ordos Basin was rich in residual oil, of which S_1 (free hydrocarbons) values ranged from 0.09 to 4.87 mg/g (average, 1.80 mg/g), and S_2 (pyrolyzed hydrocarbons) values ranged from 0.53 to 57.28 mg/g (average, 18.06 mg/g). The organic geochemistry results show that types A and B pyrites indicate shale oil enrichment and promote shale oil enrichment at >15% pyrite content. In contrast, the late-formed type C pyrite did not show shale oil enrichment.

■ AUTHOR INFORMATION

Corresponding Author

Chengfu Lyu − *Northwest Institute of Eco-Environment and Resources, Chinese Academy of Sciences/Key Laboratory of Petroleum Resources Research, Lanzhou 730000 Gansu Province, China*; Email: lyucf123@126.com

Authors

Qianshan Zhou − *Northwest Institute of Eco-Environment and Resources, Chinese Academy of Sciences/Key Laboratory of Petroleum Resources Research, Lanzhou 730000 Gansu Province, China; National Engineering Research Center of Offshore Oil and Gas Exploration, Beijing 100028, China;* ● orcid.org/0000-0002-1559-8282

Jiangyan Liu − *National Engineering Laboratory for Exploration and Development of Low Permeability Oil & Gas Fields, Xi'an 710018, China; Exploration and Development Research Institute of Changqing Oilfield Branch Company Ltd., PetroChina, Xi'an 710018, China*

Bo Ma − *Lanzhou Resources & Environment Voc-Tech University, Yellow River Basin Ecotope Integration of Industry and Education Research Institute, Lanzhou 730000, China*

Chao Li − *Northwest Institute of Eco-Environment and Resources, Chinese Academy of Sciences/Key Laboratory of Petroleum Resources Research, Lanzhou 730000 Gansu Province, China*

Yueye Xiao − *Northwest Institute of Eco-Environment and Resources, Chinese Academy of Sciences/Key Laboratory of Petroleum Resources Research, Lanzhou 730000 Gansu Province, China; University of Chinese Academy Sciences, Beijing 100049, China*

Guojun Chen − *Northwest Institute of Eco-Environment and Resources, Chinese Academy of Sciences/Key Laboratory of Petroleum Resources Research, Lanzhou 730000 Gansu Province, China*

Complete contact information is available at:
https://pubs.acs.org/10.1021/acsomega.4c00259

Notes

The authors declare no competing financial interest.

◾ REFERENCES

(1) Hakimi, M. H.; Abdullah, W. H.; Alqudah, M.; Makeen, Y. M.; Mustapha, K. A.; Hatem, B. A. Pyrolysis analyses and bulk kinetic models of the late cretaceous oil shales in jordan and their implications for early mature sulphur-rich oil generation potential. *Mar. Pet. Geol.* **2018**, *91*, 764−775.

(2) Maowen, L.; Zhijun, J.; Mingzhe, D.; Xiaoxiao, M. A.; Zhiming, L. I.; Qigui, J. I.; Yunjie, B. A.; Guoliang, T. A.; Menhui, Q. I.; Peng, L. I.; Tingting, C. A. Adcances in the basic study of lacustrine shale evolution and shale oil accumulation. *Pet. Geol. Exp.* **2020**, *42* (4), 489−505.

(3) Melek, N. C.; Plante, M.; Mine, K. Y. Resource booms and the macroeconomy: The case of U.S. shale oil. *Rev. Econ. Dyn.* **2021**, *42*, 307−332.

(4) Soeder, D. J. The successful development of gas and oil resources from shales in North America. *J. Pet. Sci. Eng.* **2018**, *163*, 399−420.

(5) Solarin, S. A. The effects of shale oil production, capital and labour on economic growth in the United States: A maximum likelihood analysis of the resource curse hypothesis. *Resour. Policy* **2020**, *68*, 101799.

(6) Zhao, W.; Zhu, R.; Hu, S.; Hou, L.; Wu, S. Accumulation contribution differences between lacustrine organic-rich shales and mudstones and their significance in shale oil evaluation. *Pet. Explor. Dev.* **2020**, *47*, 1160−1171.

(7) Zou, C. N.; Pan, S. Q.; Jing, Z. H.; Gao, J. L.; Yang, Z.; Wu, S. T.; Zhao, Q. Shale oil and gas revolution and its impact. *Acta Pet. Sin.* **2020**, *41* (1), 1−12.

(8) Zou, C. N.; Zhu, R. K.; Chen, Z. Q.; Ogg, J. G.; Wu, S. T.; Dong, D. Z.; Qiu, Z.; Wang, Y. M.; Wang, L.; Lin, S. H.; Cui, J. W.; Su, L.; Yang, Z. Organic-matter-rich shales of China. *Earth-Sci. Rev.* **2019**, *189*, 51−78.

(9) Taotao, C.; Deng, M.; Song, Z.; Liu, G.-X.; Yanran, H.; Andrew, S. H. Study on the effect of pyrite on the accumulation of shale oil and gas. *Nat. Gas Geosci.* **2018**, *29* (3), 404−414.

(10) Xu, Z. X.; Han, S. M.; Wang, Q. C. Characteristics of pyrite and its hydrocarbon significance of shale reservoir of Doushantuo Formation in middle Yangtze area. *Lithol. Reservoirs* **2015**, *27* (2), 31−37.

(11) Gu, X.; Heaney, P. J.; Reis, F. D. A. A.; Brantley, S. L. Deep abiotic weathering of pyrite. *Science* **2020**, *370*, No. eabb8092.

(12) Chabalala, V. P.; Wagner, N.; Malumbazo, N.; Eble, C. F. Geochemistry and organic petrology of the permian whitehill formation, Karoo Basin (RSA) and the Devonian/Carboniferous shale of the Appalachian Basin (USA). *Int. J. Coal Geol.* **2020**, *232*, 103612.

(13) Chen, G.; Gang, W. Z.; Liu, Y. Z.; Wang, N.; Jiang, C.; Sun, J. B. Organic matter enrichment of the Late Triassic Yanchang Formation (Ordos Basin, China) under dysoxic to oxic conditions: Insights from pyrite framboid size distributions. *J. Asian Earth Sci.* **2019**, *170*, 106−117.

(14) Lu, Z.; Tang, X.; Zhang, T.; Wang, Y.; Zhang, J.; Meng, Q.; Ma, Z.; He, Y.; Shao, D. Existence and geological significance of pyrite in the organic-rich shale of Lower Cambrain Niutitang Formation in Upper Yangtze region. *Pet. Geol. Exp.* **2021**, *43* (4), 599−610.

(15) Duan, X. G.; Xian, Y. K.; Yuan, B. G.; Dai, X.; Cao, J. J.; Liu, Z. Y.; Liu, X. Formation mechanism and formation environment of framboidal pyrite in Wufeng-Longmaxi Formation shale and its influence on shale reservoir in the southeastern Chongqing, China. *J. Chengdu Univ. Technol., Sci. Technol. Ed.* **2020**, *47* (5), 513−521.

(16) Gregory, D.; Mukherjee, I.; Olson, S. L.; Large, R. R.; Danyushevsky, L. V.; Stepanov, A. S.; Avila, J. N.; Cliff, J.; Ireland, T. R.; Raiswell, R.; Olin, P. H.; Maslennikov, V. V.; Lyons, T. W. The formation mechanisms of sedimentary pyrite nodules determined by trace element and sulfur isotope microanalysis. *Geochim. Cosmochim. Acta* **2019**, *259*, 53−68.

(17) Liu, X.; Li, A.; Fike, D. A.; Dong, J.; Xu, F.; Zhuang, G.; Fan, D.; Yang, Z.; Wang, H. Environmental evolution of the East China Sea inner shelf and its constraints on pyrite sulfur contents and isotopes since the last deglaciation. *Mar. Geol.* **2020**, *429* (1), 106307.

(18) Guangrong, Z. H.; Haikuan, N. I.; Xuan, T. A.; Wei, D.; Chuanxiang, S.; Song, C. H. Pyrite type and its effect on shale gas accumulation: a case study of Wufeng−Longmaxi shale in Sichuan Basin and its periphery. *Pet. Geol. Exp.* **2020**, *42* (3), 459−466.

(19) Song, H.; Shao, D.; Luo, H.; Meng, K.; Zhang, Y.; Tang, X.; Zhang, T. SEM image characteristics and paleoenvironmental significance of framboidal pyrite From the Lower Cambrian Shuijingtuo Formation in Yichang area, western Hubei Province, southern China: A case study of well EYY1. *Earth Sci. Front.* **2023**, *30* (3), 195−207.

(20) Lin, Z.; Sun, X.; Chen, K.; Strauss, H.; Klemd, R.; Smrzka, D.; Chen, T.; Lu, Y.; Peckmann, J. Effects of sulfate reduction processes on the trace element geochemistry of sedimentary pyrite in modern seep environments. *Geochim. Cosmochim. Acta* **2022**, *333*, 75−94.

(21) Lin, Z.; Sun, X.; Strauss, H.; Lu, Y.; Gong, J.; Xu, L.; Lu, H.; Teichert, B. M. A.; Peckmann, J. Multiple sulfur isotope constraints on sulfate-driven anaerobic oxidation of methane: Evidence from authigenic pyrite in seepage areas of the South China Sea. *Geochim. Cosmochim. Acta* **2017**, *211*, 153−173.

(22) Gong, S.; Feng, D.; Peng, Y.; Peckmann, J.; Wang, X.; Hu, Y.; Liang, Q.; Feng, J.; Chen, D. Deciphering the sulfur and oxygen isotope patterns of sulfate-driven anaerobic oxidation of methane. *Chem. Geol.* **2021**, *581*, 120394.

(23) Gong, S. G.; Peng, Y. B.; Bao, H. M.; Feng, D.; Cao, X. B.; Crockford, P. W.; Chen, D. F. Triple sulfur isotope relationships during sulfate-driven anaerobic oxidation of methane. *Earth Planet. Sci. Lett.* **2018**, *504*, 13−20.

(24) Shawar, L.; Said-Ahmad, W.; Ellis, G. S.; Amrani, A. Sulfur isotope composition of individual compounds in immature organic-rich rocks and possible geochemical implications. *Geochim. Cosmochim. Acta* **2020**, *274*, 20−44.

(25) Zhang, X.; Wu, D.; Liu, L. Characteristics and application of multiple sulfur isotopes of authigenic minerals in cold-seep environment. *Mar. Geol. Quat. Geol.* **2022**, *42* (3), 62−75.

(26) Liu, D. W.; Cai, C. F.; Hu, Y. J.; Jiang, L.; Wang, S.; Peng, Y. Y.; Li, Y. T.; Li, H. A. Hydrothermal activity temperature constrained by fractionation degree of sulfur isotope in symbiotic metal sulfide: a case study of the Lower Cambrian Longwangmiao Formation in central Sichuan Basin, China. *J. Palaeogeogr.* **2023**, *25* (1), 215−225.

(27) Siedenberg, K.; Strauss, H.; Podlaha, O.; van den Boorn, S. Multiple sulfur isotopes (δ^{34}S, Δ^{33}S) of organic sulfur and pyrite from Late Cretaceous to Early Eocene oil shales in Jordan. *Org. Geochem.* **2018**, *125*, 29−40.

(28) Raven, M. R.; Fike, D. A.; Bradley, A. S.; Gomes, M. L.; Owens, J. D.; Webb, S. A. Paired organic matter and pyrite δ^{34}S records reveal mechanisms of carbon, sulfur, and iron cycle disruption during Ocean Anoxic Event 2. *Earth Planet. Sci. Lett.* **2019**, *512*, 27−38.

(29) Jautzy, J. J.; Petts, D. C.; Clark, I. D.; Al, T. A.; Stern, R. A.; Jensen, M. Diagenetic evolution of a sedimentary system (Michigan Basin): Insights from petrography and S-isotope micro-analysis of pyrite. *Chem. Geol.* **2020**, *541*, 119580.

(30) Tarasova, Y. I.; Budyak, A. E.; Chugaev, A. V.; Goryachev, N. A.; Tauson, V. L.; Skuzovatov, S. Y.; Reutsky, V. N.; Abramova, V. D.; Gareev, B. I.; Bryukhanova, N. N.; Parshin, A. V. Mineralogical and isotope-geochemical (δ^{13}C, δ^{34}S and Pb-Pb) characteristics of the Krasniy gold mine (Baikal-Patom Highlands): Constraining ore-forming mechanisms and the model for Sukhoi Log-type deposits. *Ore Geol. Rev.* **2020**, *119*, 103365.

(31) Motomura, K.; Kiyokawa, S.; Ikehara, M.; Sano, T.; Bleeker, W.; Tanaka, K.; Miki, T.; Sano, Y. Redox fluctuation and δ^{13}Corg-δ^{34}S perturbations recorded in the 1.9 Ga Nuvilik Formation of the Cape Smith belt, Canada. *Precambrian Res.* **2021**, *359*, 106191.

(32) Eyong, J. T.; Gabriel, N.; Olive, M. C.; Jacqueline, N. A.; Moise, B.; Wignall, P.; Best, J. Sedimentary pyrite in carbonaceous shales of the Mamfe Cretaceous basin, SW Cameroon: Morphologies, composition, pyrite framboid size frequency distribution, and formation pathways. *J. Afr. Earth Sci.* **2022**, *188*, 104465.

(33) Song, L. S.; Bhattacharya, S.; Webb, Z.; Fowler, A.; Lee, V. Preservation of organic carbon in the Cretaceous Hue Shale on the North Slope of Alaska: Insights from pyrite morphology. *Int. J. Coal Geol.* **2021**, *235*, 103678.

(34) Zhao, B.; Yao, P.; Bianchi, T. S.; Wang, X. C.; Shields, M. R.; Schröder, C.; Yu, Z. Preferential preservation of pre-aged terrestrial organic carbon by reactive iron in estuarine particles and coastal sediments of a large river-dominated estuary. *Geochim. Cosmochim. Acta* **2023**, *345*, 34−49.

(35) Shawar, L.; Halevy, I.; Said-Ahmad, W.; Feinstein, S.; Boyko, V.; Kamyshny, A.; Amrani, A. Dynamics of pyrite formation and organic matter sulfurizationin organic-rich carbonate sediments. *Geochim. Cosmochim. Acta* **2018**, *241*, 219−239.

(36) Jizhen, Z.; Xianqing, L.; Yang, L. Longtan Formation shale gas reservoiring conditions and favorable region analysis in southern Sichuan area. *Coal Geol. China* **2014**, *26* (12), 1−6.

(37) Li, J.; Azmy, K. Variability of sedimentary pyrite δ^{34}S records: A case study of slope shale of the Green Point Formation in western Newfoundland, Canada. *Chem. Geol.* **2024**, *646*, 121891.

(38) Bian, R. K. The formation and evolutionary characteristics of organic matter and pyrites in the continental shales of the 3rd submember of Chang 7 Member, Yanchang formation, Ordos Basin, China. *Energy Geosci.* **2024**, *5* (2), 100250.

(39) Loucks, R. G.; Reed, R. M.; Ruppel, S. C.; Jarvie, D. M. Morphology, genesis, and distribution of nanometer-scale pores in siliceous mudstones of the Mississippian Barnett shale. *J. Sediment. Res.* **2009**, *79*, 848−861.

(40) Jingwei, C.; Rukai, Z.; Songtao, W. The effect of pyrite on the accumulation of organic matter, hydrocarbon generation and expulsion, and accumulation of oil in shale. *Geol. Rev.* **2013**, *59* (supplement), 783−784.

(41) Yuhong, L.; Hui, W.; Xiaorong, L.; Xiangzeng, W.; Yuxi, Y.; Ming, C.; Likuan, Z.; Lixia, Z.; Chengfu, J.; Chao, G. The characteristics of liquid hydrocarbon in Zhangjiatan shale, Ordos Basin and its effect on estimation of shale gas content. *Acta Petrol. Sin.* **2016**, *37* (8), 952−961.

(42) Li, K.; Zhao, Z.; Lu, H.; Liu, X.; Peng, P.; Hsu, C. S. Effects of inherent pyrite on hydrocarbon generation by thermal pyrolysis: An example of low maturity type-II kerogen from Alum shale formation, Sweden. *Fuel* **2022**, *312*, 122865.

(43) Ma, X. X.; Zheng, J. J.; Zheng, G. D.; Xu, W.; Qian, Y.; Xia, Y. Q.; Wang, Z. D.; Wang, X. F.; Ye, X. Y. Influence of pyrite on hydrocarbon generation during pyrolysis of type-III kerogen. *Fuel* **2016**, *167*, 329−336.

(44) Fu, J.; Liu, X.; Li, S.; Guo, Q.; Zhou, X.; Yang, W. Discovery and resource potential of shale oil of Chang 7 member, Triassic Yanchang Formation, Ordos Basin. *China Pet. Explor.* **2021**, *26* (5), 1−11.

(45) Fu, J.; Li, S.; Niu, X.; Deng, X.; Zhou, X. Geological characteristics and exploration of shale oil in Chang 7 Member of Triassic Yanchang Formation, Ordos Basin, NW China. *Pet. Explor. Dev.* **2020**, *47* (5), 931−945.

(46) Li, J.; Zhou, S. X.; Li, Y. J.; Ma, Y.; Yang, Y. N.; Li, C. C. Effect of organic matter on pore structure of mature lacustrine organic-rich shale: A case study of the Triassic Yanchang shale, Ordos basin, China. *Fuel* **2016**, *185*, 421−431.

(47) Li, S.; Zhu, R.; Cui, J.; Luo, Z.; Jiao, H.; Liu, H. Sedimentary Characteristics of Fine-grained Sedimentary Rock and Paleo-environment of Chang 7 Member in the Ordos Basin: A case study from Well Yaoye 1 in Tongchuan. *Acta Sedimentol. Sin.* **2019**, *38* (3), 1−3.

(48) Zhou, Q.; Zhang, D.; Li, X.; Qian, Z.; Chen, G.; Lyu, C.; Ma, X.; Li, C. Insight into the desorption behavior and mechanism of tight oil with in-situ low-temperature thermal. *J. Pet. Sci. Eng.* **2022**, *218*, 111001.

(49) Chen, R.; Liu, G.; Shang, F.; Cao, Y. Variations in hydrocarbon generating potential of the Chang 7 shale: Evidence from pyrite morphology and sulfur isotope. *J. Pet. Sci. Eng.* **2020**, *195*, 107747.

(50) Behar, F.; Beaumont, V.; Penteado, H. L. de B. Rock-Eval 6 Technology: Performances and Developments. *Oil Gas Sci. Technol.* **2001**, *56*, 111−134.

(51) Liu, D.; Yi, M.; Yang, S.; Liu, F.; Li, Y. Performance and mechanism of the pyrite-kerogen complexes oxidation with H_2O_2 at low temperature during shale stimulation: An experimental and modeling study. *Appl. Geochem.* **2022**, *143*, 105382.

(52) Ma, B.; Ji, L.; Jin, P.; Zhang, M.; Yuan, B.; Long, L. Geochemical characteristics and depositional paleoenvironment of source rocks from the Lower Cretaceous Chijinbao Formation in Jiuxi Basin, China. *J. Pet. Sci. Eng.* **2022**, *210*, 109968.

(53) Canfield, D. E.; Raiswell, R.; Westrich, J. T.; Reaves, C. M.; Berner, R. A. The use of chromium reduction in the analysis of reduced inorganic sulfur in sediments and shales. *Chem. Geol.* **1986**, *54*, 149−155.

(54) Bond, D.; Wignall, P. B. Chapter 9 Evidence for late devonian (kellwasser) anoxic events in the great basin, western United States. *Dev. Palaeontol. Stratigr.* **2005**, *20* (5), 225−262.

(55) Wang, W.; Hu, Y. L.; Muscente, A. D.; Cui, H.; Guan, C. G.; Hao, J. L.; Zhou, C. M. Revisiting Ediacaran sulfur isotope chemostratigraphy with in situ nanoSIMS analysis of sedimentary pyrite. *Geology* **2021**, *49* (6), 611−616.

(56) Peters, K. E.; Cassa, M. R. Applied source rock geochemistry. In *The Petroleum System - from Source to Trap*; Magoon, L. B., Dow, W. G., Eds.; American Association of Petroleum Geologists Memoir, 1994; Vol. *60*, pp 93−120.

(57) Shiju, L.; Misch, D.; Gao, G.; Jin, J.; Gang, W.; Yanjuan, D.; Wu, X.; Xiang, B.; Wang, M.; Luo, Q. Physical properties of lacustrine shale oil: A case study on the lower member of the Lucaogou Formation (Jimusaer Sag, Junggar Basin, NW China). *Mar. Pet. Geol.* **2022**, *145*, 105888.

(58) Zuo, Q. W.; Xu, Y. R.; Yu, B. S.; Zhang, C.; Zhang, Y. F.; Hou, C. H.; Zhang, L. H.; Sun, M. D. NanoSIMS sulfur isotope studies of pyrite from the Early Paleozoic marine shale: Implications for the sedimentary environment. *Mar. Pet. Geol.* **2021**, *124*, 104802.

(59) Uffmann, A. K.; Littke, R.; Rippen, D. Mineralogy and geochemistry of Mississippian and Lower Pennsylvanian Black Shales

at the Northern Margin of the Variscan Mountain Belt (Germany and Belgium). *Int. J. Coal Geol.* **2012**, *103*, 92−108.

(60) Wacey, D.; Noffke, N.; Cliff, J.; Barley, M. E.; Farquhar, J. Micro-scale quadruple sulfur isotope analysis of pyrite from the ~3480 Ma Dresser Formation: New insights into sulfur cycling on the early Earth. *Precambrian Res.* **2015**, *258*, 24−35.

(61) Berner, R. A. Sedimentary Pyrite Formation. *Am. J. Sci.* **1970**, *268* (1), 1−23.

(62) Liu, Q. Y.; Li, P.; Jin, Z. J.; Sun, Y. W.; Hu, G.; Zhu, D. Y.; Huang, Z. K.; Liang, X. P.; Zhang, R.; Liu, J. Y. Organic-rich formation and hydrocarbon enrichment of lacustrine shale strata: A case study of Chang 7 Member. *Sci. China: Earth Sci.* **2022**, *65* (1), 118−138.

(63) Cai, X.; Xia, W.; Liu, Y.; Liao, S.; Zhang, L.; Hu, W.; Liu, L.; Li, W.; Zeng, F. Microscopic characteristics and geological significance of pyrite in shales of the Wufeng-Longmaxi formations, southeastern Chongqing, China. *Energy Geosci.* **2024**, *5*, 100285.

(64) Li, Y. *Hydrocarbon generation characteristics and shale oil and gas potential evaluation of Chang 7 Member mud shale in Yan'an area*; Xi'an Shiyou University, 2023.